

Variations of Interstellar Gas-to-Dust Ratios at High Galactic Latitudes

J. Michael Shull

*Department of Astrophysical and Planetary Sciences, CASA
University of Colorado, Boulder, CO 80309, USA*

Georgia V. Panopoulou

*Department of Space, Earth, & Environment,
Chalmers University of Technology, SE-412 93, Gothenburg, Sweden*

michael.shull@colorado.edu, georgia.panopoulou@chalmers.se

ABSTRACT

Interstellar dust at high Galactic latitudes can influence astronomical foreground subtraction, produce diffuse scattered light, and soften the ultraviolet spectra of quasars. In a sample of 94 sight lines toward quasars at high latitude and low extinction, we evaluate the interstellar “gas-to-dust ratio” $N_{\text{H}}/E(B - V)$, using hydrogen column densities (H I and H₂) and far-infrared estimates of dust reddening. In the Galactic plane, this ratio is 6.0 ± 0.2 (in units of $10^{21} \text{ cm}^{-2} \text{ mag}^{-1}$). On average, recent Planck estimates of $E(B - V)$ in low reddening sight lines are 12% higher than those from Schlafly & Finkbeiner (2011), and N_{HI} exhibits significant variations when measured at different radio telescopes. In a sample of 51 quasars with measurements of both H I and H₂ and $0.01 \leq E(B - V) \lesssim 0.1$, we find mean ratios 10.3 ± 0.4 (gas at all velocities) and 9.2 ± 0.3 (low velocity only) using Planck $E(B - V)$ data. High-latitude H₂ fractions are generally small (2–3% on average), although 9 of 39 sight lines at $|b| \geq 40^\circ$ have f_{H_2} of 1–17%. Because FIR-inferred $E(B - V)$ is sensitive to modeled dust temperature T_d and emissivity index β , gas-to-dust ratios have large, asymmetric errors at low $E(B - V)$. The ratios are elevated in sight lines with high-velocity clouds, which contribute N_{H} but little reddening. In Complex C, the ratio decreases by 40% when high velocity gas is excluded. Decreases in dust content are expected in low-metallicity gas above the Galactic plane, resulting from grain destruction in shocks, settling to the disk, and thermal sputtering in hot halo gas.

1. Introduction

This paper examines measures of the interstellar “gas-to-dust ratio”, $N_{\text{H}}/E(B - V)$, found from the total column density of atomic and molecular hydrogen, $N_{\text{H}} = N_{\text{HI}} + 2N_{\text{H}_2}$, and selective extinction $E(B - V)$. In studies with the *Copernicus* satellite (Savage et al. 1977; Bohlin et al. 1978) hydrogen column densities were measured with UV absorption lines ($\text{Ly}\alpha$ and H_2 Lyman/Werner bands). and $E(B - V)$ was obtained from stellar photometry and spectral classification. Along 75 sight lines in the Galactic disk, they found a mean ratio $5.8 \times 10^{21} \text{ cm}^{-2} \text{ mag}^{-1}$, hereafter quoted in standard units of $10^{21} \text{ cm}^{-2} \text{ mag}^{-1}$. A recent survey with the *FUSE* satellite of sight lines to 129 OB-stars within 5 kpc (Shull et al. 2021) found a mean value 6.07 ± 1.01 (1σ variance in the distribution) using updated $E(B - V)$ from O-star photometry and spectral types from the Galactic O-star Spectroscopic Survey (Sota et al. 2011, 2014). For a subset of 21 stars at $E(B - V) \leq 0.25$ mag, the mean ratio was $N_{\text{H}}/E(B - V) = 5.83$. A *FUSE* survey of 38 translucent sight lines with $A_V \approx 0.5\text{--}4.7$ mag (Rachford et al. 2009) found a mean ratio of 5.94, and several large compilations of UV measurements found 6.12 (Gudennavar et al. 2012) and 6.2 (Liszt & Gerin 2023). We conclude that the interstellar medium (ISM) in the Galactic disk has a consistent mean gas-to-dust ratio of $\sim 6 \times 10^{21} \text{ cm}^{-2} \text{ mag}^{-1}$ to an accuracy of 3–4% and with 17% dispersion.

However, recent estimates of the gas-to-dust ratio at high Galactic latitudes find 35–45% higher values, using N_{HI} from 21-cm emission and $E(B - V)$ inferred from modeling far-infrared (FIR) emission as a tracer of the dust column. Elevated ratios above the disk plane might be expected, as dust settles gravitationally to the disk or is blown into the low halo, where it can be sputtered by hot gas. Reductions in grain abundance can also result from lower gas metallicities and grain disruption in shocks. In the radio/FIR method, values of $E(B - V)$ were taken from two studies (Schlegel et al. 1998 and Schlafly & Finkbeiner 2011) hereafter denoted SFD98 and SF11 and available on the IPAC/IRSA reddening website¹. In sight lines at latitudes $|b| > 20^\circ$ and low reddening, $0.015 < E(B - V) < 0.075$, Liszt (2014a,b) found a mean ratio $N_{\text{HI}}/E(B - V) = 8.3$, with H I from the Leiden-Argentina-Bonn (LAB) survey (Kalberla et al. 1995) at $36'$ resolution and $E(B - V)$ from SFD98. Lenz et al. (2017) found a mean ratio of 8.8, using H I from the HI4PI survey (HI4PI Collaboration et al. 2016) at $16'$ resolution and $E(B - V)$ from SF11. They only considered atomic gas with $N_{\text{HI}} < 4 \times 10^{20} \text{ cm}^{-2}$ and local standard of rest velocities $|V_{\text{LSR}}| < 90 \text{ km s}^{-1}$. Lenz et al. (2017) noted that the values obtained with the SFD98 maps are somewhat higher than the 8.3 value obtained by Liszt (2014b), who did not use the 12% SF11 correction to the SFD98 calibration. Liszt & Gerin (2023) quoted a mean high-latitude ratio of 8.3.

The question arises whether the elevated gas-to-dust-ratios at high latitude are real or the result of different methods and calibrations. To investigate the reliability of the gas-to-dust ratio $N_{\text{H}}/E(B - V)$ we examine measurements of both the numerator and denominator, considering their systematic uncertainties. Both Liszt (2014a,b) and Lenz et al. (2017) used only H I, noting

¹<https://irsa.ipac.caltech.edu/applications/DUST/docs/background.html>

that corrections for H_2 are normally small for $E(B - V) < 0.08$. This may not always be the case, as seen in our sample of quasar sight lines with both H I and H_2 data. Errors in measurements of N_{HI} can result from telescope beam sizes, stray radiation removal, baseline determination and calibration, and methods of integrating the 21-cm emission profile over velocity. Following studies by Wakker et al. (2011), we have compared N_{HI} in surveys with radio telescopes whose beam sizes range from $36'$ to $9'$, including those from the Green Bank Telescope and the HI4PI survey. We also assess the accuracy of FIR thermal emission inferences of equivalent optical extinction. Several reddening maps have been presented in the literature, exhibiting systematic differences (e.g., Lenz et al. 2017; Chiang & Ménard 2019). For example, the reddening map presented in Planck Collaboration XI (2014) has larger $E(B - V)$ at high Galactic latitude compared to SF11 (Lenz et al. 2017; Casandjian et al. 2022). All of these uncertainties result in large and asymmetric errors in the gas-to-dust ratio, especially at low reddening.

Our data set includes sight lines to 94 quasars at high Galactic latitude, most at $|b| > 25^\circ$. Indeed, 78 lie at $|b| \geq 40^\circ$. Figure 1 shows a polar projection of the quasar locations and ratios between H I column density and two FIR-inferred $E(B - V)$ maps (see Section 2.3). The H I column density has been computed within the same velocity range $[-90, 90]$ km s $^{-1}$ used to derive the gas-to-dust ratio in Lenz et al. (2017). The spatial variation of the ratio over the sky differs between the two reddening maps, indicating systematic reddening uncertainties, probably arising from FIR modeling of dust temperature and emissivity spectral index.

In Section 2 we discuss the sources of data used to evaluate the gas-to-dust ratio, including column densities N_{HI} , N_{H_2} , selective extinction $E(B - V)$, and their uncertainties. We examine the measurements used to construct $N_{\text{H}}/E(B - V)$ ratios along the sight lines to 94 high-latitude quasars. In particular, we explore uncertainties in 21-cm measurements of N_{HI} from different radio telescopes and uncertainties in inferring $E(B - V)$ from FIR emission and grain emissivity models. In Section 3 we present data from our survey, which confirm previous observations of elevated gas-to-dust ratios at $|b| > 30^\circ$. However, we suggest large uncertainties in the ratio. An important effect in elevated ratios is the reduced dust content in Galactic high velocity clouds (HVCs) and some intermediate velocity clouds (IVCs). In Section 4, we summarize our results and their implications for astronomical foreground subtraction, diffuse scattered light, and reddening corrections for the ultraviolet spectra of quasars. We stress the importance of identifying the systematic uncertainties in $\log N_{\text{H}}$ and $E(B - V)$, which are almost certainly much larger than the small values ($\leq 5\%$) commonly listed in observational tables.

2. Data Compilation for Gas-to-Dust Ratios

Our full sample includes 94 quasars at high Galactic latitude (Table 1). The first 55 quasars listed (group 1) have both H I and H_2 column densities, a primary sample that includes 47 sight lines with IVCs and 18 with HVCs. Nine AGN lie behind Complex C (Figure 2), an extended structure of high-velocity gas with metallicities 10–30% solar (Wakker et al. 1999; Collins et al. 2007; Shull

et al. 2011). We also analyzed 39 additional quasars (group 2 in Table 1) in which only H I column densities were available. In contrast to UV studies of H I and H₂ in the Galactic disk, the high-latitude measurements of the dust-to-gas ratio (Liszt 2014a,b; Lenz et al. 2017) used 21-cm emission for N_{HI} and FIR emission as a proxy for $E(B - V)$. As described in Appendix A, these techniques can introduce systematic errors in the gas-to-dust ratio, particularly when $E(B - V) \lesssim 0.04$ mag. Toward high-latitude quasars, reddening uncertainties often dominate the propagated errors in the ratio $N_{\text{HI}}/E(B - V)$. However, we also found cases in which measurements of N_{HI} differ by 10–30% among different telescopes with a range of beam sizes.

We use two reddening maps based on previous modeling of the thermal dust emission: (1) recalibration of the SFD98 map by SF11; (2) the map presented in Planck Collaboration XLVIII (2016). The 2016 Planck map employed the GNILC technique (Generalized Needlet Internal Linear Combination) which uses spatial information from angular power spectra and diffuse component separation to reduce contamination by cosmic infrared background radiation. These values are preferred over those from Planck-DL (Planck Collaboration XXIX 2016). Values of $E(B - V)$ for both SFD98 and SF11 are available on the IPAC/IRSA reddening website. Although that website quotes both values, we only list SF11 values, which are 86% of SFD98 owing to re-calibration of colors using stars from the Sloan Digital Sky Survey². The SF11 study found that the SFD98 map needed a re-calibration by a factor 0.86 (0.865 in their Table 6 for the CTIO-V filter). The map has a FWHM of 6.1'. We query this map using the IPAC/IRSA website, which provides 1σ variances averaged over neighboring 5' pixels around each line of sight. We also downloaded the original SFD98 map projected into a HEALPix grid of $N_{\text{side}} = 2048$ and applied the re-calibration correction factor³.

We investigated shifts in the gas-to-dust ratio when we use $E(B - V)$ from Planck-GN (Planck Collaboration XLVIII 2016) instead of SF11. For the 48 AGN sight lines with $E(B - V) \leq 0.02$, the GN reddenings are 15% higher than SF11 on average (15 are lower, 33 are higher). For the 81 AGN with $E(B - V) \leq 0.04$, the GN reddenings are 12% higher on average. Thus, using GN reddening instead of SF11 would reduce the gas-to-dust ratios by 11–13%. For the 11 sight lines with $E(B - V) < 0.01$, the ratio reductions are even larger. In Table 1, we highlight these uncertain sight lines in boldface (four in group 1, seven in group 2).

²The re-calibrated SF11 values of $E(B - V)$ are 86% those of SFD98, but were not applied by Liszt (2014b). The 0.86 factor is less than the conversion factor described in Section 2.2.1 of Lenz et al. (2017) where 0.884 is for the Landolt-V filter, and 0.865 is for the CTIO-V filter. Lenz et al. (2017) also noted a mean ratio $N_{\text{HI}}/E(B - V) = 8.2$, using pixels in a revised reddening map (Schlafly et al. 2014) based on Pan-STARRS1 optical photometry of 500 million stars.

³The map is provided on `lambda.gsfc.nasa.gov` by Chiang (2023).

2.1. Atomic Hydrogen (N_{HI})

The H I column densities came from 21-cm spectra in several surveys. All 94 AGN appear in the H I compilation of Wakker et al. (2003), who published velocity profiles from a variety of radio telescopes, primarily the Green Bank 140-ft (GB), 100-m Green Bank Telescope (GBT), Leiden-Dwingeloo Survey, Effelsberg, and Villa Elisa. This 2003 paper has been used in many studies of interstellar gas (metallicities, H_2 , and ionized phases) because it contains velocity-component fits to the emission profiles. This allows to keep separate accounts of low-velocity H I and HVCs and IVCs, when present. However, Gaussian fitting can sometimes give spurious total column densities.

We also study these sight lines using the HI4PI all-sky survey, which combined data from the Effelsberg and Parkes radio telescopes with an angular resolution of $16'$ (HI4PI Collaboration et al. 2016). We use two related data products: (a) the N_{HI} map computed by integrating the H I spectra over the entire velocity range of $|V_{\text{LSR}}| < 600 \text{ km s}^{-1}$; and (b) the N_{HI} map obtained by Lenz et al. (2017) who integrated over low-velocity gas, $|V_{\text{LSR}}| < 90 \text{ km s}^{-1}$ excluding HVC emission, and masked out regions with $N_{\text{HI}} > 4 \times 10^{20} \text{ cm}^{-2}$. We refer to the former as NHI–HI4PI(all) and the latter as NHI–HI4PI(90). Both maps are provided in HEALPix with $N_{\text{side}} = 1024$.

Liszt (2014a,b) used H I column densities from the LAB survey ($36'$ beam), and Lenz et al. (2017) used the HI4PI survey ($16.1'$). For the H I column densities and 21-cm spectra presented by Wakker et al. (2003) the beams range from $35'$ in the Leiden-Dwingeloo Survey (Hartmann & Burton 1997) to $16.1'$ with the Parkes Telescope and 9 – $10'$ (GBT and Effelsberg). A large beam could include small-scale H I, and velocity component fitting could be more difficult. These should not be major issues at high latitudes except in cases of small-scale structure. Nevertheless, there is a potential mismatch to the resolutions of the space-borne telescopes: IRAS (4 – $5'$ at $100 \mu\text{m}$) and Planck ($5'$ at 350 – $857 \mu\text{m}$). With its $9.1'$ beam and avoidance of stray radiation due to its off-axis mount, the GBT should provide reliable column densities. This was the conclusion in a previous comparison (Wakker et al. 2011) who also identified 10% offset in N_{HI} from data taken in the LAB survey, owing to a “spurious broad component” with $N_{\text{HI}} \approx 5 \times 10^{19} \text{ cm}^{-2}$.

In Table 2 we compare N_{HI} measured by radio telescopes with various beam sizes toward 36 AGN in common with those tabulated by Wakker et al. (2011). The column densities in Table 1 (from Wakker et al. 2003) are higher on average by $+0.059$ (dex) in $\log N_{\text{HI}}$ relative to those from GBT. Columns from the GB 140-ft are higher by $+0.017$ (dex), and those from the HI4PI survey are higher by $+0.023$ (dex). Quoted measurement errors in $\log N_{\text{HI}}$ are typically ± 0.01 – 0.03 . We consider differences $\Delta \log N_{\text{HI}} \geq 0.050$ to be discrepant and highlight them in boldface. Figure 3 shows the differences in N_{HI} between HI4PI and Wakker et al. (2003). Although the average offset differences are comparable to the quoted errors on $\log N_{\text{HI}}$, several AGN sight lines (e.g., 3C 273, Mrk 279, Mrk 335, Mrk 1383, PG 1259+593, PG 0953+414, Ton S180) exhibit somewhat larger offsets (0.05 – 0.12 dex). These include 5 of 32 sight lines measured by both GBT and HI4PI.

Systematic errors in N_{HI} could arise from calibration, stray-radiation contamination, or small-scale structure influenced by beam size. Integration of antenna temperature over the 21-cm velocity

profile could also result in variations in the total column density. This may be the case in complex 21-cm profiles such as Mrk 279 and PG 1259+593. Reducing the H I column densities by 12–15% would lower the gas-to-dust ratios, as would increasing $E(B - V)$ in low reddening sight lines.

2.2. Molecular Hydrogen (N_{H_2})

Of the 94 quasars in our survey, 55 quasars (group 1) have both H I and H₂ column densities. The H₂ column densities were measured by FUSE far-ultraviolet (FUV) absorption-line spectra. With some survey overlap, these came from 45 sight lines in Gillmon et al. (2006), 18 in Wakker (2006), and one each from Richter et al. (2001b), Collins et al. (2003), and Fox et al. (2005). Notes on overlapping H₂ data from these surveys and corrections for specific sight lines are provided in Appendix B. In most of the 55 sight lines, the H₂ column densities are much smaller than those of H I. In 30 of the 39 AGN sight lines at latitudes $|b| \geq 40^\circ$, the molecular fraction $f_{\text{H}_2} \equiv 2N_{\text{H}_2}/N_{\text{H}}$ ranges between 3×10^{-6} and 5×10^{-4} , often making H₂ a negligible contributor to the total N_{H} in sight lines with column densities below the atomic-to-molecular transition at $\log N_{\text{H}} \approx 20.38 \pm 0.13$ seen at high latitude (Gillmon et al. 2006). However, nine sight lines at $|b| \geq 40^\circ$ have $f_{\text{H}_2} > 0.01$ (range 1–17%) and are listed in Table 3, together with $\log N_{\text{H}}$ and $E(B - V)$. These 9 sight lines have $E(B - V) = 0.02\text{--}0.06$ (SF11 scale), which is below the observed H I-to-H₂ transition at $E(B - V) \approx 0.08\text{--}0.10$ seen in low-latitude surveys (Bohlin et al. 1978; Shull et al. 2021). Shifts in the transition to lower N_{H} toward high-latitude quasars are influenced by lower gas metallicities, lower dust content, and reduced far-UV (H₂-dissociating) radiation fields; see Browning et al. (2003) and Gillmon et al. (2006) for models.

We also analyzed 39 additional quasars (group 2 in Table 1) in which only H I column densities were available. Because these AGN are all at $|b| \geq 40^\circ$ with $E(B - V) < 0.056$, the H₂ contributions could be small in most cases. However, 17 of the 39 sight lines have column densities $\log N_{\text{H}} \approx 20.25\text{--}20.67$, near or above the H I-to-H₂ transition. Thus, some of the group-2 sample would likely require corrections (1% to 10%) for undetected H₂. In our Tables, we separate the two groups (55 and 39 AGN) and conduct independent statistical analyses.

2.3. Reddening Maps

The dust optical depth map presented in Planck Collaboration XLVIII (2016) was obtained by modeling the Galactic thermal dust emission and separating contributions from the Cosmic Infrared Background (CIB). The GNILC method was applied to the Planck 2015 data and the IRAS 100 μm map. The final optical depth map has a $5'$ beam size and is provided at HEALPix $N_{\text{side}} = 2048$ resolution. We multiply the optical depth map at 353 GHz by the conversion factor 1.49×10^4 to obtain $E(B - V)$ in magnitudes. Henceforth, we will refer to these techniques as Planck-GN, and the reddening map as the GN map. When comparing to N_{HI} maps from HI4PI and Lenz et al.

(2017) we smooth the reddening maps to 16.1' resolution to match the H I data. As discussed in Appendix E of Planck Collaboration XI (2014), the choice of filter used to compute $E(B-V)$ affects the conversion from dust emission to reddening. The Planck team used the filter transmission of the Johnson photometric system (M.-A. Miville-Deschênes, private communication). The recalibration factor of SFD98 in this system is 0.884, as used in Lenz et al. (2017).

Toward the AGN at high Galactic latitude and low extinction, the inferred values of $E(B-V)$ have large uncertainties, and may in fact be underestimated. For the quasars in our sample, the mean (FIR-inferred) values from SFD98 and SF11 are low: $E(B-V) = 0.030$ for group 1 (55 quasars) and 0.019 for group 2 (39 quasars). Figure 4 compares differences in $E(B-V)$ between Planck-GN and SF11 values. On average, the Planck-GN values are 12% larger than those from SF11 towards the AGN in our sample, including those for the nine Complex C sight lines (plotted in red). Because of their improvement over previous Planck products, we use the GN maps, which were recommended for thermal dust science. The visual extinction is often estimated as $A_V = R_V E(B-V)$, with a commonly adopted value of $R_V = 3.1$. This adds further systematic uncertainty, as Peek & Schiminovich (2013) found that no single value of R_V is valid over the entire high-latitude sky.

Using FIR emission from foreground dust to estimate the equivalent optical reddening requires sophisticated models of the grain temperature and emissivity (e.g., Draine & Li 2007; Compiègne et al. 2011; Hensley & Draine 2021) which depend on grain composition, size distribution, and solid-state properties. In Appendix C we discuss the dependence of FIR (353 GHz) optical depth and dust radiance on the dust temperature (T_d) and emissivity index (β), where emissivity $\epsilon(\nu) \propto \nu^\beta$. Combining the scaling of dust radiance $\mathcal{R} \propto \tau_{353} T_d^{4+\beta} \propto T_d^{3+\beta}$ with the observed anti-correlation ($\beta \propto T_d^{-\alpha}$), we find that radiance is sensitive to small changes in the two parameters (α, β),

$$\frac{\mathcal{R}}{\mathcal{R}_0} = \left(\frac{\beta}{\beta_0} \right)^{-(3+\beta)/\alpha}. \quad (1)$$

Table 4 shows the dust parameters adopted in several FIR papers. Over the range of indices, $\beta = 1.6 \pm 0.2$, adopted in the 2016 Planck-GNLC study and with $\alpha = 2/3$, the radiance factor would change by a factor of 2.3 about \mathcal{R}_0 . Table 5 lists the 100 μm surface brightness $I(100 \mu\text{m})$, FIR-modeled dust temperature T_d , and inferred color excess, $E(B-V)$ from SF11. The listed error bars are 1σ variances in $E(B-V)$ over neighboring 5' pixels. The true uncertainties are likely much larger. Column 4 lists $I(100 \mu\text{m})/E(B-V)$, with errors propagated from relative errors on $I(100 \mu\text{m})$ and $E(B-V)$ added in quadrature. Several AGN sight lines have large relative errors on $E(B-V)$ and $I(100 \mu\text{m})$, with $I(100 \mu\text{m})/E(B-V)$ uncertain by 10-15%. The surface brightnesses typically range from 0.4-2 MJy sr⁻¹, with mean values 1.61 MJy sr⁻¹ (first group of 55) and 1.07 MJy sr⁻¹ (second group of 39). The mean dust temperatures are $\langle T_d \rangle = 17.900$ K (17.912, 17.892) and the mean ratios are $\langle I(100 \mu\text{m})/E(B-V) \rangle = 56.22$ MJy sr⁻¹ mag⁻¹ (56.24, 56.20). Here, the first values are for all 94 quasars, and the numbers in parentheses denote the means for groups 1 and 2. The uniformity in mean dust temperatures is

surprising, with 1σ variance $\sigma(T_d) = 0.213$ K (1.2% in group 1). The correspondence between FIR flux and reddening is good, with 10% variance $\sigma(I/E) = 5.63$ MJy sr⁻¹ mag⁻¹ in the distribution of $I(100 \mu\text{m})/E(B - V)$. However, because of the sensitivity of the modeled dust column density to T_d and β , small changes can alter the inferred $E(B - V)$.

Given the uncertainties in the dust modeling, the systematic errors on $E(B - V)$ are likely much larger than those quoted in the IPAC/IRSA tables (1σ variances). For these reasons, we are suspicious of the accuracy of the ratios $N_{\text{H}}/E(B - V)$ for AGN sight lines with $E(B - V) \lesssim 0.04$. In the next section, we examine these issues statistically for various sub-samples.

3. Survey Results

Table 1 presented the gas column densities, inferred $E(B - V)$, and corresponding ratio $N_{\text{H}}/E(B - V)$. All 94 quasars are lightly reddened, with $E(B - V)$ extending from 0.005 to 0.110 (SF11 scale). The first group of 55 quasars with both H I and H₂ column densities has mean $E(B - V) = 0.030$, while the second group (H I only) has mean $E(B - V) = 0.019$. The difference likely arises from the somewhat higher latitudes in the second group. In group 1, we combine molecular hydrogen column densities N_{H_2} with those of atomic hydrogen N_{HI} to arrive at the total hydrogen column density $N_{\text{H}} = N_{\text{HI}} + 2N_{\text{H}_2}$. Columns 9 and 10 in Table 1 list dust-to-gas ratios for gas at all velocities and for low-velocity gas only.

In Section 3.1 we discuss the statistical changes of excluding these sight lines in modified sub-samples (51 in group 1 and 32 in group 2). In Section 3.2, we compare the gas-to-dust ratios in sight lines that contain HVCs and IVCs. In Section 3.3 we discuss Planck all-sky maps of dust extinction and differences from earlier studies.

3.1. Gas-to-Dust Ratios for QSO Sub-samples

Table 6 shows mean values of the ratios $N_{\text{H}}/E(B - V)$ for sub-samples of the 94 high-latitude QSOs. The first group includes the 55 quasars for which we have both H I and H₂ column densities. The second group includes 39 quasars with only H I. In each group, we list two mean ratios: one for all H I velocity components fitted by Wakker et al. (2003) and a second for low-velocity gas with $|V_{\text{LSR}}| < 90$ km s⁻¹. Elevated ratios are evidence that dust grains are deficient in high-velocity gas. For the 55 quasars, the mean ratio using Planck-GN values of $E(B - V)$ is 11% higher than SF11. For the 39 quasars in group 2, the mean ratio for Planck-GN is 12% higher. In the low-velocity statistics we excluded all HVCs and most of the IVCs, except for 17 IVCs in well-known structures containing H₂ and included with low-velocity gas. The two modified sub-samples in Table 6 omit the 11 sight lines with highly uncertain $E(B - V) \leq 0.01$. The mean ratios of the sub-samples and excluded sight lines are listed for comparison.

Figure 5 plots the 55 (group 1) individual gas-to-dust ratios vs. $E(B-V)$. Some of the elevated ratios are unreliable because of large reddening uncertainties at $E(B-V) \leq 0.04$. The two values of reddening in the IPAC/IRSA tables (SFD98 and SF11) differ by 14% because of recalibration. Systematic differences in $E(B-V)$ can arise because of FIR modeling sensitivity to dust parameters (T_d , β) as discussed in Appendix C. Gas-to-dust ratios appear high in HVCs because of low grain content, which adds H I column density to the sight line without dust reddening. It remains unclear whether the dust deficiency arises from low metallicity or grain disruption in shocks (or both). Low dust content in HVCs and IVCs was also noted in the Planck papers, for example Section 6.3 of Planck Collaboration XXIV (2011), and in Figures 4 and 5 in Lenz et al. (2017) that illustrate the dependence of $N_{\text{HI}}/E(B-V)$ on H I velocity. Their range of ratios is even larger than found here, probably due to different sky selections.

Complex C is a good example of HVC effects, demonstrating the importance of keeping separate account of the high velocity gas. Table 7 shows the gas-to-dust ratios for nine quasar sight lines passing through this gaseous structure. The last four columns list the ratios derived for gas at all velocities and then omitting H I in the HVCs. The ratios are shown for $E(B-V)$ taken from both SF11 and Planck-GN. In both cases, the mean gas-to-dust ratios drop 40% when one excludes HVCs. In Complex C, gas velocity is a major factor in the elevated ratios.

Table 7 also illustrates differences in $E(B-V)$ estimates from SF11 and Planck-GN among the Complex C sight lines. On average, the Planck-GN estimate is 23% higher than SF11, over a range in SF11 reddening from $E(B-V) = 0.0053$ to 0.0344. The three sight lines with $E(B-V) < 0.010$ are likely quite uncertain, resulting in large, asymmetric errors on $N_{\text{HI}}/E(B-V)$. For example, PG 1626+554 has $\log N_{\text{HI}} = 20.053$ (all velocities) and 19.936 (low-velocity gas) but with different values of $E(B-V) = 0.0053$ (SF11) and 0.0137 (GN). Adopting the GN reddening instead of SF11 reduces $N_{\text{HI}}/E(B-V)$ from 21.3 to 8.24 (all-velocities) and from 16.3 to 6.28 (low-velocity gas). Similarly, toward Mrk 817, where $\log N_{\text{HI}} = 20.085$ (all velocities), $E(B-V) = 0.0059$ (SF11), and 0.0115 (GN), the gas-to-dust ratio drops by a factor of two, using GN instead of SF11.

3.2. Distinguishing Low-Velocity and High-Velocity Gas

Here we examine the possibility of different grain abundances in high velocity gas. Specifically, we explore the dust-to-gas ratios after excluding HVCs and some IVCs. To distinguish low-velocity gas from higher velocity clouds, we tabulated the column densities of the velocity components and performed statistics with and without HVC/IVC gas. This allowed us to assess whether some of the gas is deficient in dust as a result of grain processing in interstellar shocks (Draine & Salpeter 1979; Seab & Shull 1983; Jones et al. 1996; Slavin et al. 2004). The H I column densities in Table 1 (columns 5 and 6) were determined by summing the Gaussian component fits (Wakker et al. 2003) in the 21-cm spectra.

Most of the HVCs (Wakker & van Woerden 1997) with velocities $|V_{\text{LSR}}| \geq 90 \text{ km s}^{-1}$ in the

local standard of rest show no evidence for dust, probably because of reduced metallicity or shock destruction of grains. In some sight lines, HVCs provide a sizable portion of the 21-cm emission (Wakker et al. 2003; Collins et al. 2007; Shull et al. 2011; Martin et al. 2015; Panopoulou & Lenz 2020). IVCs have broadly been classified (Albert & Danly 2004) as having $|V_{\text{LSR}}|$ between 20–90 km s⁻¹. In recent surveys, the IVC ranges were chosen as 30–90 km s⁻¹ (Richter et al. 2003) and 40–90 km s⁻¹ (Lehner et al. 2022). Located in the lower Galactic halo, IVCs display a variety of physical conditions, with gas metallicities near solar values (Wakker 2001; Richter et al. 2001a, 2003), but refractory element abundances that suggest some grain disruption.

From the 21-cm spectra of our sample, we grouped the H I emission components into three velocity categories: HVCs ($|V_{\text{LSR}}| \geq 90$ km s⁻¹), IVCs ($|V_{\text{LSR}}| = 30\text{--}90$ km s⁻¹), and low-velocity gas. In the first group of 55 AGN sight lines with both H I and H₂ data, we identified HVCs in 18 quasar sight lines (33% coverage) and IVCs in 39 sight lines (73% coverage). In the second group of 39 quasars with only H I data, we identified HVCs toward 3 quasars (8%) and IVCs toward 27 quasars (69%). The difference in HVC incidence may be an effect of the higher Galactic latitudes of the AGN in group 2. Nine of the quasars in group 1 were targeted to study HVC Complex C. In addition, high-latitude absorbers may be more ionized, with spatial extents greater than those seen in H I. Previous UV studies of IVC/HVC ionized gas in the strong Si III 1206.500 Å absorption line found large sky-covering fractions, $f_c = 0.81 \pm 0.05$ (Shull et al. 2009) and $f_c = 0.77 \pm 0.06$ (Richter et al. 2017).

FIR emission has been observed in some IVCs (e.g., Planck Collaboration XXIV 2011; Planck Collaboration XI 2014), and the infrared cirrus was shown to correlate with H₂ absorption (Gillmon & Shull 2006). In our statistical analysis of velocity effects, we included 17 strong IVCs with the low-velocity gas. These sight lines are marked by asterisks in column 10 of Table 1. We excluded all HVCs and most IVCs from the column densities of low velocity gas. The excluded IVCs have velocities well separated from the low-velocity 21-cm emission near the LSR. Included with the low-velocity gas were 10 of the 39 IVCs in group 1, and 7 of the 27 IVCs in group 2. They are all well-known structures: eight sight lines through the Intermediate Velocity Arch (IV Arch), three through the S1 cloud, four through IV18, and one each through IV19 and IV26.

Planck Collaboration XXIV (2011) noted that IVCs had different FIR properties, with different emission cross sections, often 50% lower compared to the low-velocity clouds. There is also evidence for grain disruption in intermediate velocity absorbers, including the “Routly-Spitzer effect” (Routly & Spitzer 1952) in which elevated Ca II/Na I ratios are observed at increasing cloud velocity. Similar effects are observed in the rising abundances of refractory elements (Si, Fe) with increasing cloud velocity (Shull et al. 1977). There has been no strong evidence for dust emission in HVCs (e.g., Wakker & Boulanger 1986; Désert et al. 1988) other than an unconfirmed claim of IR emission in one HVC (Miville-Deschênes et al. 2005). Fox et al. (2023) reported indirect evidence for some dust in Complex C, based on sub-solar differential abundance ratios of refractory elements (Fe/S, Si/S, Al/S) relative to sulfur, which is assumed to be undepleted. Similar depletion measurements have been seen in the Leading Arm of the Magellanic Stream (Richter et al. 2018).

3.3. All-Sky Maps

The sight lines through Complex C suggest that both low dust content and uncertainties in FIR estimates of $E(B - V)$ could be responsible for some of the elevated ratios along high latitude sight lines with low reddening. We have compared the SF11 estimates of $E(B - V)$ to values from Planck Collaboration XLVIII (2016) denoted here as Planck-GN. Polar projection maps in Figure 6 illustrate the differences, which often track changes in the gas-to-dust ratio in the maps of Figure 1. Features in the Northern Galactic hemisphere that appear yellow in the GN ratio map correlate with locations of IVCs, where both SFD98 and SF11 overestimate the total reddening compared to Planck-GN. The bright feature in red near the North Galactic Pole at $(\ell, b) = (260 - 330^\circ, 80 - 84^\circ)$ is Markkanen’s cloud (Markkanen 1979). This feature is also known as the North Galactic Pole Rift, seen in H I (Puspitarini & Lallement 2012) and appearing as a foreground shadow in X-rays (Snowden et al. 2015). This region is known (Planck Collaboration XI 2014) to have a low dust emission spectral index (β) compared to the rest of the high-latitude sky. It shows up in the reddening difference map because SFD98 assumed a constant β , whereas Planck-GN fit for the emission index.

Figure 7 shows three distributions of gas-to-dust ratios, using different values of $E(B - V)$. The three colored curves show $N_{\text{HI}}/E(B - V)$ for low-velocity H I, with $E(B - V)$ taken from the SF11 re-calibration (blue), SFD recalibrated with 0.884 (orange), and Planck-GN (green). We find mean ratios of 9.3 (SF11) and 8.6 (Planck) in units of $10^{21} \text{ cm}^{-2} \text{ mag}^{-1}$. The two vertical (dotted, dashed) lines show the mean high-latitude ratios (8.8 and 8.2) quoted in Lenz et al. (2017). The two vertical solid lines show the Galactic disk-plane values (5.8 and 6.07) from Bohlin et al. (1978) and Shull et al. (2021).

4. Summary and Conclusions

The goal of our study was to assess the accuracy and reliability of measurements of the gas-to-dust ratio $N_{\text{HI}}/E(B - V)$ toward high-latitude extragalactic sources. Using radio/FIR techniques, past studies (Liszt 2014a,b; Lenz et al. 2017; Liszt & Gerin 2023) found 35–45% higher ratios than established values in the Galactic disk plane. There are many astrophysical processes that could segregate dust from gas (Hensley & Draine 2021; Shull et al. 2021) to produce a deficit of interstellar dust grains above the disk plane. Dust could settle to the disk, be radiatively elevated into the halo, or be transported by supernova-driven outflows. Most HVCs exhibit little or no evidence for dust, either because of low metallicity or shock destruction. Dust elevated above the Galactic plane will come into contact with hot gas, with grain sputtering lifetimes of $t_{\text{sp}} \approx (1 \text{ Gyr})(10^{-3} \text{ cm}^{-3}/n_e)$ at $10^{6.0-6.5} \text{ K}$.

Observations of gas and dust at high and low Galactic latitudes employ different methods and calibrations. In the Galactic disk surveys, the hydrogen (H I, H₂) column densities were measured from UV absorption toward OB-type stars, with $E(B - V)$ inferred from stellar photometry and

intrinsic colors assigned to spectral classification. Most high-latitude gas measurements employ H I 21-cm emission toward extragalactic targets, and $E(B - V)$ is inferred from models that convert FIR dust emission to the corresponding optical extinction. In some cases, H₂ measurements are available toward AGN, but often not.

From our survey of 94 AGN, we confirm previous observations of elevated gas-to-dust ratios at high Galactic latitude (Liszt 2014a,b; Lenz et al. 2017). However, we found systematic uncertainties in measurements of both the numerator N_{HI} and denominator $E(B - V)$ of the ratio. The different ratios found with the two techniques are seen primarily at high latitudes and in sight lines with $E(B - V) \leq 0.04$. From sub-samples of the 94 AGN, examining the measurements N_{HI} , N_{H_2} , and $E(B - V)$, we came to several conclusions about offsets and uncertainties:

- Values of $E(B - V)$ from Planck-GN generally exceed those from SF11 towards the AGN in our sample. On average, we found their ratio (GN/SF11) to be 15% higher for 48 AGN with $E(B - V) \leq 0.02$ and 12% higher for 81 AGN with $E(B - V) \leq 0.04$.
- Measurements with the GBT 100 m telescope exhibit N_{HI} lower by 4.0–4.5% on average compared to the NRAO 140 ft at Green Bank and the HI4PI survey. In several sight lines, GBT measured N_{HI} lower by 10–30%.
- Including H₂ in the total $N_{\text{H}} = N_{\text{HI}} + 2N_{\text{H}_2}$ increases N_{H} by 2–3% on average at high latitude, with four sight lines exhibiting f_{H_2} of 7% to 17%.
- Excluding high velocity gas (HVCs) decreases $N_{\text{H}}/E(B - V)$ by 15% on average, and by 40% for nine sight lines through Complex C.

Figure 8 visually illustrates the mean gas-to-dust ratios in our sub-samples. For each sub-sample, three points show the shifts that occur when one uses different reddening maps (SF11 vs. Planck-GN) or sight lines with values of N_{HI} at all velocities or just low velocity. Within formal uncertainties, our dust-to-gas ratios are consistent with the 8.8 value from Lenz et al. (2017) when we exclude the low-reddening sight lines, consider gas at all velocities, and use Planck-GN reddening. The right-most points in each triplet in Figure 8 (labeled SF11, low) are also consistent with Lenz et al. (2017), but that sub-sample only considers low-velocity gas. There is also good evidence that Planck-GN reddening maps are superior to SF11. The mean ratio is sensitive to the AGN sample selection, implying once again that the formal variation about the mean underestimates the systematic uncertainties.

As noted, surveys of extragalactic targets at $|b| > 30^\circ$ would be expected to show higher gas-to-dust ratios. However, it is important to assess how much arises from reduced grain content, and how that deficiency occurs. High ratios are clearly seen in sight lines with HVCs (18 of 55 of the AGN sight lines in group 1). In this sample with both H I and H₂ measurements, the mean ratio drops by 15% when HVCs are excluded. Some of the anomalously high ratios may result from under-estimated reddening when $E(B - V) \leq 0.04$. A comparison of H I column densities obtained

from different radio telescopes (Table 2) found differences in N_{HI} between GB and GBT telescopes and from the HI4PI survey, as well as from LAB, LDS, and Effelsberg measurements. Uncertainties in $E(B - V)$ may be even larger, as converting FIR emission to optical reddening requires precise modeling of dust temperature T_d and grain emissivity index β . Appendix C demonstrated the sensitivity of dust radiance to β and its anti-correlation with T_d . We also discussed the accuracy of $E(B - V)$ in previous FIR studies (SFD98, SF11) compared to values from FIR all-sky maps from the Planck Mission. Tabulated values of $E(B - V)$ at $|b| > 30^\circ$ have systematic uncertainties larger than the variances listed on the IPAC/IRSA website. Given the sensitivity of the FIR-derived values to grain parameters, the optical extinction may be underestimated in high-latitude AGN sight lines.

We now summarize our survey results for the mean ratios of gas-to-dust,

1. In the Galactic disk, the mean ratio $N_{\text{HI}}/E(B - V)$ of interstellar gas-to-dust in the Galactic disk has been determined as 6.0 ± 0.2 (in units of $10^{21} \text{ cm}^{-2} \text{ mag}^{-1}$) by many studies (Bohlin et al. 1978; Shull et al. 2021; Gudennavar et al. 2012; Liszt & Gerin 2023). For 51 quasars at high Galactic latitude, with both H I and H₂ and $0.01 \leq E(B - V) \lesssim 0.1$ (Planck-GN scale), we find mean ratios 10.3 ± 0.4 (gas at all velocities) and 9.2 ± 0.3 (low-velocity).
2. A portion of the high gas-to-dust ratios likely arises from reduced grain content in HVCs (and some IVCs) owing to low metallicity and shock destruction of grains. For nine sight lines passing through Complex C, with mean $E(B - V) = 0.0151$ (SF11) and 0.0185 (GN), the ratio decreases by 40% when high velocity gas is excluded.
3. Owing to uncertainties in both numerator N_{HI} and denominator $E(B - V)$, the gas-to-dust ratio has large and asymmetric errors. In a comparison of 36 AGN sight lines, some values of $\log N_{\text{HI}}$ differed by 0.05–0.12 (dex) in 21-cm observations at various radio telescopes. Compared to data from the GBT 100 m (9.1' beam), the average values of $\log N_{\text{HI}}$ were higher by +0.017 (GB-140 ft, 21' beam), +0.023 (HI4PI, 16' beam), and +0.059 Wakker et al. (2003).
4. Elevated $N_{\text{HI}}/E(B - V)$ may also arise from uncertain FIR estimates of $E(B - V)$, which are sensitive to dust temperature T_d and emissivity index β . With their observed anti-correlation, $(\beta/\beta_0) = (T_d/T_0)^{-\alpha}$, dust radiance $\mathcal{R} \equiv \int I_\nu d\nu$ depends sensitively on the emissivity index, $\mathcal{R}/\mathcal{R}_0 = (\beta/\beta_0)^{-(3+\beta)/\alpha}$. For $\alpha \approx 2/3$ (Martin et al. 2012) and $\beta = 1.6 \pm 0.2$ adopted in the 2016 Planck-GN study, factor-of-two changes could occur in $E(B - V)$ from variations about the fitted radiance \mathcal{R}_0 .
5. Values of $E(B - V)$ at $|b| > 30^\circ$ from Planck-GN dust emission are preferred over those from Planck-DL, SF11, or SFD98. On average, Planck-GN reddening values are 12% higher than SF11 for $E(B - V) \leq 0.04$, with large variations in the (GN/SF11) ratios of $E(B - V)$. An underestimate of reddening at high latitudes and low $E(B - V)$ is consistent with an analysis of Planck data (Casandjian et al. 2022), who also found excess dust at high latitude.

Reddening maps and variations in the gas-to-dust ratio are important for studies of the ISM and many other areas of astrophysics. Owing to the steep rise of selective extinction toward shorter wavelengths, the spectral slopes of de-reddened UV spectra of AGN will be harder than found in composite spectra (Stevens et al. 2014) which used IPAC/IRSA reddening tables. Reddening maps will affect CMB foreground subtraction and derivation of cosmological parameters, including “B-modes” in polarized emission. Variations in $\log N_{\text{HI}}$ measurements and FIR-inferred $E(B - V)$ and propagated errors in the numerator and denominator result in large, asymmetric errors in $N_{\text{HI}}/E(B - V)$. This suggests the need to obtain high-quality 21-cm observations of a sample of high-latitude quasars to understand the source of offsets. It would also be helpful to update the IPAC/IRSA reddening tables, frequently used to convert measured N_{HI} to reddening and extinction.

We thank Jean-Marc Cassandjian, Bruce Draine, Charles Danforth, Andrew Fox, Brandon Hensley, and Bart Wakker for helpful discussions, and Harvey Liszt for a thorough and timely referee report. Jay Lockman and Bart Wakker kindly provided additional 21-cm data from the Green Bank Telescope and expert advice on several AGN sight lines. Marc-Antoine Miville-Deschênes provided the optical filter bandpasses used in the Planck analysis. A portion of this study was supported by the New Horizons Mission observational planning for observations of cosmic backgrounds at high Galactic latitude. The authors also acknowledge Interstellar Institute’s Program II6 and the Paris-Saclay University’s Institut Pascal for hosting discussions that nourished the development of the ideas behind this work. Our survey made use of the reddening website for IPAC/IRSA data of FIR emission and modeled values of dust temperature T_d and $E(B - V)$.

REFERENCES

- Albert, C. E., & Danly, L. 2004, in *High Velocity Clouds*, ASSL, 312, 73, ed. H. van Woerden, B. P. Wakker, U. J. Schwarz, K. S. de Boer (Dordrecht: Kluwer Acad. Publ.)
- Bohlin, R. C., Savage, B. D., & Drake, J. F. 1978, *ApJ*, 224, 132
- Browning, M. K., Tumlinson, J., & Shull, J. M. 2003, *ApJ*, 582, 810
- Casandjian, J.-M., Ballet, J., Grenier, I., & Remy, Q. 2022, *ApJ*, 940, 116
- Chiang, Y.-K. 2023, arXiv:2306.03926
- Chiang, Y.-K., & Ménard, B. 2019, *ApJ*, 870, 120
- Collins, J. A., Shull, J. M., & Giroux, M. L. 2003, *ApJ*, 585, 336
- Collins, J. A., Shull, J. M., & Giroux, M. L. 2007, *ApJ*, 657, 271
- Compiègne, M., Verstraete, L., Jones, A., et al. 2011, *A&A*, 525, A103
- Désert, F. X., Bazell, D., & Boulanger, F. 1988, *ApJ*, 334, 815
- Draine, B. T., & Li, A. 2007, *ApJ*, 657, 810

- Draine, B. T., & Salpeter, E. E. ApJ, 231, 438
- Fox, A. J., Savage, B. D., Wakker, B. P., et al. 2005, ApJ, 630, 332
- Fox, A. J., Cashman, F. H., Kriss, G. A., et al. 2023, ApJ, 946, L48
- Gillmon, K., & Shull, J. M. 2006, ApJ, 636, 908
- Gillmon, K., Shull, J. M., Tumlinson, J., & Danforth, C. 2006, ApJ, 636, 891
- Górski, K. M., Hivon, E., Banday, A.J., et al. 2005 ApJ 622, 759
- Gudennavar, S. B., Bubbly, S. G., Preethi, K., & Murthy, J. 2012, ApJS, 199, 8
- Hartmann, D., & Burton, W. B. 1997, Atlas of Galactic Neutral Hydrogen (Cambridge: Cambridge University Press)
- Hensley, B. S., & Draine, B. T. 2021, ApJ, 906, 73
- HI4PI Collaboration, Ben Bekhti, N., Floer, L., et al. 2016, A&A, 594, A116
- Jones, A. P., Tielens, A. G. G. M., & Hollenbach, D. J. 1996, ApJ, 469, 740
- Kalberla, P. M. W., Burton, W. B., Hartmann, D., et al. 1995, A&A, 440, 775.
- Lehner, N., Howk, J. C., Marasco, A., & Fraternali, F. 2022, MNRAS, 513, 3228
- Lehner, N., Savage, B. D., Wakker, B. P. et al. 2006, ApJS, 164, 1
- Lenz, D., Hensley, B. S., & Doré, O. 2017, ApJ, 846, 38
- Liszt, H. 2014a, ApJ, 780, 10
- Liszt, H. 2014b, ApJ, 783, 17
- Liszt, H., & Gerin, M. 2023, ApJ, 943, 172
- Markkanen, T. 1979, A&A, 74, 201
- Martin, P. G., Blagrove, K. P. M., Lockman, F. J., et al. 2015, ApJ, 809, 153
- Martin, P. G., Roy, A., Bontemps, S., et al. 2012, ApJ, 751, 28
- Meisner, A. M., & Finkbeiner, D. P. 2015, ApJ, 798, 88
- Miville-Deschênes, M.-A., Boulanger, F., et al. 2005, ApJ, 631, L57
- Panopoulou, G. V., & Lenz, D. 2020, ApJ, 902, 120
- Paradis, D., Veneziani, M., Noriega-Crespo, A., et al. 2010, A&A, 540, L8
- Peek, J. E. G., & Schiminovich, D. 2013, ApJ, 771, 68
- Planck Collaboration XXIV 2011, A&A, 536, A24
- Planck Collaboration XI 2014, A&A, 571, A11
- Planck Collaboration XXIX 2016, A&A, 586, A132 (Planck-DL)
- Planck Collaboration XLVIII 2016, A&A, 596, A109 (Planck-GN)
- Planck Collaboration IV 2020, A&A, 641, A4

- Puspitarini, L., & Lallement, R. 2012, *A&A*, 545, A21
- Rachford, B. L., Snow, T. P., Destree, J. D., et al. 2009, *ApJS*, 180, 125
- Routly, P. M., & Spitzer, L. 1952, 115, 227
- Richter, P., Fox, A. J., Wakker, B. P., et al. 2018, *ApJ*, 865, 145
- Richter, P., Nuza, S. E., Fox, A. J., et al. 2017, *A&A*, 607, A48
- Richter, P., Sembach, K. R., Wakker, B. P., et al. 2001a, *ApJ*, 559, 318
- Richter, P., Sembach, K. R., Wakker, B. P., & Savage, B. D. 2001b, *ApJ*, 562, L181
- Richter, P., Wakker, B. P., Savage, B. D., & Sembach, K. R. 2003, *ApJ*, 586, 230
- Savage, B. D., Bohlin, R. C., Drake, J. F., & Budich, W. 1977, *ApJ*, 216, 291
- Schlafly, E. F., & Finkbeiner, D. P. 2011, *ApJ*, 737, 103 (SF11)
- Schlafly, E. F., Green, G., Finkbeiner, D.P., et al. 2014, *ApJ*, 786, 29
- Schlegel, D. J., Finkbeiner, D. P., & Davis, M. 1998, *ApJ*, 500, 525 (SFD98)
- Seab, C. G., & Shull, J. M. 1983, *ApJ*, 275, 652
- Shull, J. M., & Danforth, C. W. 2019, *ApJ*, 882, 180
- Shull, J. M., Danforth, C. W., & Anderson, K. L. 2021, *ApJ*, 911, 55
- Shull, J. M., Stevans, M., Danforth, C. W., et al. 2011, *ApJ*, 739, 105
- Shull, J. M., Jones, J. R., Danforth, C. W., & Collins, J. A. 2009, *ApJ*, 699, 754
- Shull, J. M., York, D. G., & Hobbs, L. M. 1977, *ApJ*, 211, L139
- Slavin, J. D., Dwek, E., & Jones, A. P. 2004, *ApJ*, 803, 7
- Snowden, S. L., Koutroumpa, D., Kuntz, K. D., et al. 2015, *ApJ*, 806, 120
- Sota, A., Maíz Apellániz, J., Walborn, N. R., et al. 2011, *ApJS*, 193, 24
- Sota, A., Maíz Apellániz, J., Morrell, N. I., et al. 2014, *ApJS*, 211, 10
- Stevans, M. L., Shull, J. M., Danforth, C. W., & Tilton, E. M. 2014, *ApJ*, 794, 75
- Wakker, B. P. 2001, *ApJS*, 136, 463
- Wakker, B. P. 2006, *ApJS*, 163, 282
- Wakker, B. P., & Boulanger, F. 1986, *A&A*, 170, 84
- Wakker, B. P., Howk, J. C., Savage, B. D., et al. 1999, *Nature*, 402, 388
- Wakker, B. P., Lockman, F. J., & Brown, J. M. 2011, *ApJ*, 728, 159
- Wakker, B. P., Savage, B. D., Sembach, K. D., et al. 2003, *ApJS*, 146, 1
- Wakker, B. P., & van Woerden, H. 1997, *ARA&A*, 35, 217

A. Error Propagation in the Ratio $N_{\text{H}}/E(B-V)$

Errors in the gas-to-reddening ratio $N_{\text{H}}/E(B-V)$ arise from uncertainties in measurements of three quantities: $\log N_{\text{HI}}$, $\log N_{\text{H}_2}$, and E_{B-V} , where $N_{\text{H}} \equiv N_{\text{HI}} + 2N_{\text{H}_2}$. Because $\log N = (\ln N/2.303)$, we have $\sigma_{\log N_{\text{H}}} = (\sigma_{\ln N_{\text{H}}}/2.303) = (\sigma_{N_{\text{H}}}/2.303 N_{\text{H}})$. The propagated errors on $\log N_{\text{H}}$ give the weighted formula,

$$\sigma_{\log N_{\text{H}}}^2 = \left(\frac{N_{\text{HI}}}{N_{\text{H}}}\right)^2 \sigma_{\log N_{\text{HI}}}^2 + \left(\frac{2N_{\text{H}_2}}{N_{\text{H}}}\right)^2 \sigma_{\log N_{\text{H}_2}}^2. \quad (\text{A1})$$

Similarly, propagated errors in $N_{\text{H}}/E(B-V)$ lead to

$$\left(\frac{\sigma_{\text{ratio}}}{\text{ratio}}\right)^2 = \left(\frac{\sigma_{N_{\text{H}}}}{N_{\text{H}}}\right)^2 + \left(\frac{\sigma_{E_{B-V}}}{E_{B-V}}\right)^2 = \left[2.303 \sigma_{\log N_{\text{H}}}\right]^2 + \left[\frac{\sigma_{E_{B-V}}}{E_{B-V}}\right]^2. \quad (\text{A2})$$

We can use this expression to evaluate which errors dominate uncertainty in the gas-to-reddening ratios discussed in this paper. Consider a typical example of O-star data (Shull & Danforth 2019) for HD 15137 (O9.5 II-III_n) at $b = -7.58^\circ$ with $\log N_{\text{HI}} = 21.24 \pm 0.07$, $\log N_{\text{H}_2} = 20.27 \pm 0.05$, and $E(B-V) = 0.35 \pm 0.03$. Here, the molecular fraction $f_{\text{H}_2} = 0.186$, the total hydrogen column density $\log N_{\text{H}} = 21.324 \pm 0.058$, and the ratio is $N_{\text{H}}/E(B-V) = (6.02 \pm 0.96) \times 10^{21} \text{ cm}^{-2} \text{ mag}^{-1}$ with uncertainty $\sigma_{\text{ratio}}/\text{ratio} = 0.159$ (16% errors). Errors on the ratio are dominated by uncertainties in $\log N_{\text{HI}}$ [0.07 dex or 17%] and $\log N_{\text{H}_2}$ (0.05 dex or 12%) compared to 9% error on $E(B-V)$. Consider now an O-star sight line with lower reddening, $E(B-V) = 0.15 \pm 0.03$ (20% error) and column densities $\log N_{\text{HI}} = 21.00 \pm 0.05$ and $\log N_{\text{H}_2} = 19.24 \pm 0.10$. In this case, $\log N_{\text{H}} = 21.015 \pm 0.048$ (12% errors) and the ratio is $(6.90 \pm 1.58) \times 10^{21}$ with 23% errors. In this case, errors on $E(B-V)$ are more important.

Next, consider a moderately reddened quasar, Mrk 1095 with $\log N_{\text{HI}} = 20.969 \pm 0.07$, $\log N_{\text{H}_2} = 18.76_{-0.31}^{+0.21}$, and $E(B-V) = 0.1099$. The IPAC/IRSA tables quote an error of ± 0.0017 (1.5%) on $E(B-V)$ (from SF11), but we suggest a larger systematic error of ± 0.02 (18%). From these, we find $\log N_{\text{H}} = 20.974 \pm 0.069$ and $\sigma_{\text{ratio}}/\text{ratio} = 0.24$, so that $N_{\text{H}}/E(B-V) = (6.8 \pm 1.6) \times 10^{21} \text{ cm}^{-2} \text{ mag}^{-1}$. Errors on this ratio are dominated by uncertainties in both $\log N_{\text{HI}}$ (17%) and $E(B-V)$ (18%).

As a final example, consider Mrk 279, a high-latitude quasar behind Complex C with low reddening (see Table 7) variously quoted as $E(B-V) = 0.0161 \pm 0.0006$ (SFD98), 0.0138 ± 0.0005 (SF11), 0.0197 ± 0.0063 (Planck-DL), and 0.0154 ± 0.0002 (Planck-GN). The column densities are $\log N_{\text{HI}} = 20.388 \pm 0.05$, $\log N_{\text{H}_2} = 14.42 \pm 0.09$, and $\log N_{\text{H}} = 20.338 \pm 0.048$. The gas-to-dust ratios (15.8, 11.1, 14.1) are given in the usual (10^{21}) units. The quoted relative errors on $E(B-V)$ are inconsistent with the 26% dispersion among the three estimates; systematic errors likely dominate the uncertainty on the ratio. Similar uncertainties (and bias) are likely present in other lightly reddened extragalactic sight lines.

B. Notes on H₂ for Individual AGN Sight Lines

In Table 1, we listed H₂ column densities for the 55 sight lines in group 1 based on several sources, primarily two 2006 FUSE surveys of high-latitude quasars (Gillmon et al. 2006; Wakker 2006). We found generally good agreement, but in several cases there were discrepancies. Table 1 includes H₂ column densities for 38 of the 45 AGN in Gillmon et al. (2006). For 9 other sight lines (H1821+643, HE 0226-4110, Mrk 501, Mrk 817, NGC 1399, NGC 3310, NGC 3690, NGC 4214, PHL 1811) we adopted values from Wakker (2006), who analyzed additional FUSE observations and generated smaller error bars. Wakker (2006) also provided H₂ data for 9 additional targets (H1821+643, HE 0226-4110, Mrk 279, Mrk 501, Mrk 817, Mrk 1383, NGC 985, PG 1116+215, Ton S210). Table 3 in that paper also lists line widths (FWHM), which we translate to $b = \text{FWHM}/1.665$ (assuming a Gaussian profile) to compare with curve-of-growth Doppler parameters found by Gillmon et al. (2006). Below are notes on several discrepancies and our reasons for the selected N_{H_2} .

Fairall 9. Richter et al. (2001b) detected H₂ with $\log N_{\text{H}_2} = 16.40^{+0.28}_{-0.53}$ in the Magellanic Stream toward Fairall 9 at $V_{\text{LSR}} = +190 \text{ km s}^{-1}$. No H₂ was seen at low velocity (Gillmon et al. 2006). We quote the high-velocity value, $\log N_{\text{H}_2} = 16.40$ in Table 1.

H1821+643. Published H₂ column densities and Doppler parameters differ between two FUSE surveys: $\log N_{\text{H}_2} = 17.91^{+0.13}_{-0.20}$ with $b = 1.7^{+0.8}_{-0.7} \text{ km s}^{-1}$ (Gillmon et al. 2006) and $\log N_{\text{H}_2} = 15.99^{+0.16}_{-0.06}$ based on $b = 4.3 \text{ km s}^{-1}$ inferred from $\text{FWHM} = 7.2 \text{ km s}^{-1}$ quoted in Table 3 of Wakker (2006). The difference arises from the two curve-of-growth b -values (or FWHM) fitted to the data. We adopted the lower columns of Wakker (2006) because his higher Doppler parameter seemed more plausible physically.

HE 0226-4110. Gillmon et al. (2006) quoted $\log N_{\text{H}_2} < 14.29$, but Fox et al. (2005) detected $\log N_{\text{H}_2} = 14.58 \pm 0.09$. Two subsequent analyses quoted 14.54 (Lehner et al. 2006) and $14.56^{+0.15}_{-0.10}$ (Wakker 2006). Summing the column densities $N(J)$ for $J = 0-3$ in Table 3 of Wakker (2006), we find $\log N_{\text{H}_2} = 14.60 \pm 0.14$, with propagation of errors on $N(J)$. We use the latter value in Table 1.

MRC 2251-178. Gillmon et al. (2006) quoted $\log N_{\text{H}_2} = 14.54^{+0.23}_{-0.17}$, based on a detection in $J = 1$ and an upper limit in $J = 0$. Wakker (2006) listed a total column density $\log N_{\text{H}_2} = 15.02^{+0.45}_{-0.23}$, but that included upper limits for column densities in $J = 2-4$, which should probably not be included in the total sum. Instead, we adopt $\log N_{\text{H}_2} = 14.87^{+0.23}_{-0.17}$ from the detected column densities in $J = 0$ and $J = 1$.

Mrk 106. Gillmon et al. (2006) quoted $\log N_{\text{H}_2} = 16.23^{+0.21}_{-0.15}$ with $b = 14.9^{+3.5}_{-2.6} \text{ km s}^{-1}$. Wakker (2006) quoted $\log N_{\text{H}_2} = 18.54^{+0.11}_{-0.10}$ with $\text{FWHM} = 7.5 \text{ km s}^{-1}$ ($b = 4.5 \text{ km s}^{-1}$). We adopt the smaller column density, since the high value in Wakker (2006) should produce detectable damping wings. (However, the FUSE data do not have high S/N.) Another argument for the lower value is that a large H₂ column density and high molecular fraction ($f_{\text{H}_2} \approx 0.03$) would be unlikely at the estimated $E(B - V) \approx 0.0235$ (SF11).

Mrk 279. This target did not appear in Gillmon et al. (2006). Wakker (2006) mentioned no low-velocity H₂ absorption, but his Table 4 listed $\log N_{\text{H}_2} = 14.42 \pm 0.09$ in the LLIV arch at $V_{\text{LSR}} = -41 \text{ km s}^{-1}$. We quote the latter (IVC) value in Table 1.

Mrk 501. We adopted the value $\log N_{\text{H}_2} = 15.49_{-0.24}^{+0.66}$ from Wakker (2006), as it was based on additional data than used by Gillmon et al. (2006).

Mrk 817. We adopted the value $\log N_{\text{H}_2} = 14.48_{-0.07}^{+0.08}$ from Wakker (2006), as it was based on additional data than used by Gillmon et al. (2006).

Mrk 876. Gillmon et al. (2006) quoted $\log N_{\text{H}_2} = 16.58$ (low-velocity) and 15.75 (IVC at -33 km s^{-1}) both seen in $J = 0-3$. The fitted Doppler parameters were $b = 7.3 \text{ km s}^{-1}$ and 5.7 km s^{-1} respectively. Wakker (2006) found a much higher column density for the low-velocity component, $\log N_{\text{H}_2} = 18.07_{-0.22}^{+0.22}$ with FWHM = 7.6 km s^{-1} ($b = 4.6 \text{ km s}^{-1}$), but a similar value to Gillmon et al. (2006), $15.47_{-0.13}^{+0.39}$, for the IVC component. We adopt the Gillmon et al. (2006) values, since the high value in Wakker (2006) might produce detectable damping wings. (The FUSE data do not have high S/N.) Such a large molecular fraction ($f_{\text{H}_2} \approx 0.014$) would be unlikely at the estimated $E(B - V) \approx 0.0230$ (SF11).

Mrk 1383. We adopted the value $\log N_{\text{H}_2} = 14.78_{-0.14}^{+0.20}$ from Wakker (2006), as it was based on additional data than used by Gillmon et al. (2006) and had smaller errors on $N(J)$.

NGC 985. The two FUSE surveys find similar values, $\log N_{\text{H}_2} = 16.05_{-0.33}^{+1.95}$ (Gillmon et al. 2006) and $\log N_{\text{H}_2} = 16.07_{-0.24}^{+0.77}$ (Wakker 2006). We list the latter value (smaller errors).

PG 1116+215. Gillmon et al. (2006) quoted upper limits on low-velocity H₂ in $J = 0$ and $J = 1$, with $\log N(0) < 13.78$ and $\log N(1) < 13.93$. Wakker (2006) quoted an upper limit $\log N(0) < 13.79$ but detected $\log N(1) = 13.82_{-0.22}^{+0.20}$ in the low-velocity component. He also quoted H₂ detections in the S1 IVC (-44 km s^{-1}) with $\log N_{\text{H}_2} = 15.27_{-0.23}^{+0.44}$. However, summing the column densities $N(J)$ for $J = 0-3$ in Wakker (2006), we find $\log N_{\text{H}_2} = 16.01_{-0.27}^{+0.38}$, with errors propagated $\log N(J)$. We quote the latter (IVC) value in Table 1.

Ton S210. The FUSE surveys find different values, $\log N_{\text{H}_2} = 16.57_{-1.38}^{+1.18}$ (Gillmon et al. 2006) with $b = 4.4_{-2.4}^{+5.6} \text{ km s}^{-1}$ and $\log N_{\text{H}_2} = 15.61_{-0.20}^{+0.32}$ (Wakker 2006) with FWHM = 7.3 km s^{-1} ($b = 4.4 \text{ km s}^{-1}$). We list the latter in Table 1 (additional data analyzed).

C. Sensitivity of $E(B - V)$ Estimates to Dust Modeling

The FIR-inferred values of optical selective extinction $E(B - V)$ are derived from a chain of computations and correlations with dust optical depth or integrated emission intensity. Figure 14 of Lenz et al. (2017) is instructive, showing systematic differences between reddening maps as a function of dust temperature. The values from Planck Collaboration papers (2011, 2014, 2016, 2020) employ parameterized models of thermal dust emission based on a modified blackbody (MBB)

model with emissivity $\epsilon(\nu) \propto \nu^\beta$. The parameters are based on assumed grain composition (e.g., graphite + silicates), size distributions, and emission properties (e.g., Draine & Li 2007; Compiegne et al. 2011). Most past studies assumed a single-temperature dust distribution, with $T_d \approx 16\text{--}23$ K and $\beta \approx 1.5\text{--}2.0$. Meisner & Finkbeiner (2015) explored a two-component model with “hot dust” ($T_d \approx 16.2$ K, $\beta = 1.67$) and “cold dust” ($T_d \approx 9.15$ K, $\beta = 2.70$).

The observed determinations of the β -index (Table 4) illustrate the difficulties in dust modeling. An early study (Planck Collaboration XXIV 2011) used $\beta = 1.8$, noting compatibility with the FIRAS spectrum of the diffuse ISM. Subsequent Planck papers found $\beta \approx 1.6$ for high-latitude sight lines. Their mean and 1σ variance were $\beta = 1.59 \pm 0.12$ (Planck Collaboration XI 2014) and $\beta = 1.63 \pm 0.17$ (Planck Collaboration XLVIII 2016). Several of these studies used a “dust radiance” method to estimate the thermal dust emission in a MBB model, with radiance defined as

$$\mathcal{R} = \int I_\nu d\nu = \int \tau_{353} B_\nu(T_d) \left(\frac{\nu}{353 \text{ GHz}} \right)^\beta d\nu \propto \tau_{353} T_d^{4+\beta}. \quad (\text{C1})$$

Here τ_{353} is the dust optical depth at $\nu_0 = 353$ GHz, the frequency at which the emissivity index is normalized. In the MBB formulation, with $\tau_\nu = I_\nu/B_\nu$ and $B_\nu(T_d) = (2\nu^2 T_d/c^2)$ in the Rayleigh-Jeans limit, the dust optical depth $\tau_{353} \propto T_d^{-1}$. Because of the sensitivity of dust emissivity to temperature, it is useful to understand how the inferred radiance depends on the assumed index β . Several papers (see Figure 16 in Planck Collaboration XI 2014) found an anti-correlation between β_{obs} and T_{obs} . A possible explanation is that when dust emits more efficiently it acquires a lower temperature.

Martin et al. (2012) proposed an approximate relation, $(\beta/1.8) \approx (T_d/17.9 \text{ K})^{-2/3}$, based on 100–500 μm Galactic-plane data from Paradis et al. (2010). The latter paper fitted to a general relation, $\beta \propto T_d^{-\alpha}$ and $\alpha \approx 4/3$ (with substantial scatter). We adopt the formulation $(\beta/\beta_0) = (T_d/T_0)^{-\alpha}$, where T_0 and β_0 are fiducial parameters chosen at the center of the distributions. Combining the scaling of $\mathcal{R} \propto \tau_{353} T_d^{4+\beta} \propto T_d^{3+\beta}$ with the anti-correlation ($T_d \propto \beta^{-1/\alpha}$) between dust emission index and dust temperature, we find that radiance is quite sensitive to changes in these indices (α and β),

$$\frac{\mathcal{R}}{\mathcal{R}_0} = \left(\frac{\beta}{\beta_0} \right)^{-(3+\beta)/\alpha}. \quad (\text{C2})$$

For the range of emission indices, $\beta = 1.6 \pm 0.2$, adopted in the 2016 Planck-GN study (and $\alpha = 2/3$) the radiance factor changes by a factor of 2.3 about \mathcal{R}_0 . Over the range of adopted indices (Table 5) the differences could be even larger.

Table 1. Data on 94 AGN Sight Lines and their “Gas-to-Dust” Ratios^a

AGN Name	ℓ (deg)	b (deg)	$E(B - V)$ (SF11)	$\log N_{\text{HI}}^{\text{b}}$ (all-v)	$\log N_{\text{HI}}^{\text{b}}$ (low-v)	$\log N_{\text{H}_2}^{\text{b}}$ (FUSE)	$\log N_{\text{H}}^{\text{b}}$ (total)	Ratio ^c (all-v)	Ratio ^c (low-v)	GN-Ratio ^c (all-v)
(1)	(2)	(3)	(4)	(5)	(6)	(7)	(8)	(9)	(10)	(11)
3C 249.1	130.39	38.55	0.0301 ± 0.0020	20.446	20.335	18.98 ^{+0.12} _{-0.14}	20.475	9.92	7.82	7.48
3C 273	289.95	64.36	0.0179 ± 0.0004	20.222	20.222	15.72 ^{+0.13} _{-0.09}	20.222	9.32	9.32	8.02
ESO 141-G55	338.18	-26.71	0.0944 ± 0.0062	20.788	20.704	19.32 ^{+0.07} _{-0.07}	20.817	6.95	5.80	7.05
Fairall 9	295.07	-57.83	0.0217 ± 0.0011	20.526	20.383	16.40 ^{+0.28} _{-0.53}	20.526	15.5	11.1	15.5
H1821+643	94.00	27.42	0.0370 ± 0.0007	20.584	20.570	15.99 ^{+0.16} _{-0.06}	20.584	10.4	10.0	10.0
HE 0226-4110	253.94	-65.77	0.0132 ± 0.0005	20.272	20.272	14.60 ^{+0.14} _{-0.14}	20.272	14.2	14.2	11.6
HE 1143-1810	281.85	41.71	0.0331 ± 0.0005	20.506	20.496	16.54 ^{+1.32} _{-0.68}	20.506	9.69	9.46	9.12
HS 0624+6907	145.71	23.35	0.0845 ± 0.0021	20.898	20.798	19.82 ^{+0.09} _{-0.09}	20.964	10.9	8.97	8.66
MRC 2251-178	46.20	-61.33	0.0335 ± 0.0011	20.415	20.407	14.54 ^{+0.23} _{-0.17}	20.415	7.77	7.61	10.3
Mrk 9	158.36	28.75	0.0503 ± 0.0015	20.677	20.639	19.36 ^{+0.09} _{-0.08}	20.717	10.4	9.57	7.88
Mrk 106	161.14	42.88	0.0235 ± 0.0010	20.453	20.349	16.22 ^{+0.21} _{-0.15}	20.453	12.1	9.50	9.13
Mrk 116	160.53	44.84	0.0292 ± 0.0028	20.505	20.429	19.09 ^{+0.08} _{-0.09}	20.537	11.8	10.0	8.30
Mrk 205	125.45	41.67	0.0344 ± 0.0011	20.508	20.405	16.53 ^{+0.13} _{-0.37}	20.508	9.37	7.38	8.54
Mrk 209	134.15	68.08	0.0122 ± 0.0005	20.052	20.006	< 14.48	20.052	9.24	8.30*	8.35
Mrk 279	115.04	46.86	0.0138 ± 0.0005	20.338	19.926	14.42 ^{+0.09} _{-0.24}	20.338	15.8	6.11	14.2
Mrk 290	91.49	47.95	0.0120 ± 0.0008	20.426	20.125	16.18 ^{+0.49} _{-0.39}	20.426	22.2	11.1	16.4
Mrk 335	108.76	-41.42	0.0305 ± 0.0031	20.567	20.428	18.83 ^{+0.08} _{-0.08}	20.583	12.5	9.23	9.56
Mrk 421	179.83	65.03	0.0130 ± 0.0011	20.166	19.936	14.63 ^{+0.09} _{-0.10}	20.166	11.3	6.64	11.5
Mrk 478	59.24	65.03	0.0111 ± 0.0009	20.010	19.963	< 14.56	20.010	9.22	8.28	9.74
Mrk 501	63.60	38.86	0.0164 ± 0.0003	20.314	20.242	15.49 ^{+0.66} _{-0.24}	20.314	12.6	10.6	11.3
Mrk 509	35.97	-29.86	0.0492 ± 0.0005	20.613	20.577	17.87 ^{+0.31} _{-0.78}	20.614	8.36	7.71	8.36
Mrk 817	100.30	53.48	0.0059 ± 0.0002	20.085	19.950	14.48 ^{+0.08} _{-0.07}	20.085	20.6	15.1*	10.6
Mrk 876	98.27	40.38	0.0230 ± 0.0009	20.424	20.210	16.58 ^{+1.96} _{-0.42}	20.424	11.5	7.05	9.14
Mrk 1095	201.69	-21.13	0.1099 ± 0.0017	20.969	20.969	18.76 ^{+0.21} _{-0.31}	20.975	8.62	8.62	9.96
Mrk 1383	349.22	55.12	0.0276 ± 0.0009	20.547	20.547	14.78 ^{+0.20} _{-0.14}	20.547	12.8	12.8	15.2
Mrk 1513	63.67	-29.07	0.0370 ± 0.0017	20.555	20.525	16.42 ^{+1.08} _{-0.26}	20.555	9.70	9.06	7.98
MS 0700.7+6338	152.47	25.63	0.0448 ± 0.0014	20.609	20.609	18.75 ^{+0.27} _{-0.68}	20.620	9.31	9.31	8.48
NGC 985	180.84	-59.49	0.0282 ± 0.0003	20.522	20.522	16.07 ^{+0.77} _{-0.33}	20.522	11.8	11.8	13.6
NGC 1068	172.10	-51.93	0.0289 ± 0.0004	20.436	20.416	18.13 ^{+0.13} _{-0.17}	20.440	9.53	9.11	8.56
NGC 1399	236.72	-53.63	0.0109 ± 0.0004	20.196	20.196	< 14.55	20.196	14.4	14.4	10.7
NGC 1705	261.08	-38.74	0.0070 ± 0.0005	20.251	20.119	< 14.17	20.251	25.5	18.8	18.7
NGC 3310	156.60	54.06	0.0192 ± 0.0005	20.150	19.888	19.14 ^{+0.22} _{-0.42}	20.227	8.78	8.78*	6.08
NGC 3690	141.91	55.41	0.0144 ± 0.0002	19.994	19.758	< 14.40	19.994	6.85	6.47*	6.37
NGC 4151	155.08	75.06	0.0237 ± 0.0011	20.322	20.284	16.70 ^{+0.93} _{-0.31}	20.322	8.86	8.86*	11.3
NGC 4214	160.24	78.07	0.0187 ± 0.0003	20.232	19.538	15.22 ^{+0.31} _{-0.19}	20.232	9.12	9.12*	11.2
NGC 4670	212.69	88.63	0.0128 ± 0.0003	20.040	19.951	14.72 ^{+0.13} _{-0.16}	20.040	8.56	6.98	9.79
NGC 7469	83.10	-45.47	0.0599 ± 0.0015	20.649	20.646	19.67 ^{+0.10} _{-0.10}	20.732	9.00	8.94	7.59
NGC 7714	88.22	-55.56	0.0451 ± 0.0002	20.674	20.636	18.94 ^{+0.05} _{-0.05}	20.690	10.9	10.0	8.20
PG 0804+761	138.28	31.03	0.0302 ± 0.0005	20.588	20.545	18.66 ^{+0.14} _{-0.13}	20.598	13.1	11.9	10.4
PG 0844+349	188.56	39.97	0.0314 ± 0.0007	20.475	20.475	18.22 ^{+0.18} _{-0.28}	20.480	9.62	9.62	11.3
PG 0953+414	179.79	51.71	0.0102 ± 0.0006	20.087	20.004	15.03 ^{+0.11} _{-0.10}	20.087	12.0	9.90	10.1
PG 1116+215	223.36	68.21	0.0193 ± 0.0001	20.075	19.705	16.01 ^{+0.44} _{-0.33}	20.075	6.16	6.16*	14.1
PG 1211+143	267.55	74.32	0.0286 ± 0.0011	20.421	20.249	18.38 ^{+0.15} _{-0.14}	20.429	9.39	9.39*	12.6
PG 1259+593	120.56	58.05	0.0070 ± 0.0004	20.225	19.669	14.75 ^{+0.10} _{-0.12}	20.225	24.0	11.2*	19.5

Table 1—Continued

AGN Name	ℓ	b	$E(B - V)$	$\log N_{\text{HI}}^{\text{b}}$	$\log N_{\text{HI}}^{\text{b}}$	$\log N_{\text{H}_2}^{\text{b}}$	$\log N_{\text{H}}^{\text{b}}$	Ratio ^c	Ratio ^c	GN-Ratio ^c
(1)	(deg)	(deg)	(SF11)	(all-v)	(low-v)	(FUSE)	(total)	(all-v)	(low-v)	(all-v)
PG 1302-102	308.59	52.16	0.0376 ± 0.0009	20.502	20.368	$15.62^{+1.41}_{-0.16}$	20.502	8.44	8.41	8.69
PG 1351+640	111.89	52.02	0.0177 ± 0.0003	20.441	20.286	$18.34^{+0.20}_{-0.11}$	20.448	15.9	11.2*	18.0
PG 1626+554	84.51	42.19	0.0053 ± 0.0005	20.053	19.936	$15.14^{+0.54}_{-0.20}$	20.053	21.3	16.3	8.24
PHL 1811	47.46	-44.81	0.0415 ± 0.0031	20.592	20.592	$19.36^{+0.07}_{-0.06}$	20.640	10.5	10.5	6.10
PKS 0405-12	204.93	-41.76	0.0503 ± 0.0036	20.537	20.537	$15.79^{+0.25}_{-0.12}$	20.537	6.85	6.85	8.54
PKS 0558-504	257.96	-28.57	0.0388 ± 0.0012	20.675	20.526	$15.44^{+0.18}_{-0.12}$	20.675	12.2	8.66	9.92
PKS 2005-489	350.37	-32.60	0.0479 ± 0.0007	20.655	20.600	$15.07^{+0.10}_{-0.10}$	20.655	9.43	8.31	12.9
PKS 2155-304	17.73	-52.25	0.0185 ± 0.0005	20.123	20.123	$14.17^{+0.11}_{-0.14}$	20.123	7.17	7.17	12.5
Ton S180	139.00	-85.07	0.0123 ± 0.0002	20.097	20.083	< 14.37	20.097	10.2	9.84	13.8
Ton S210	224.97	-83.16	0.0144 ± 0.0004	20.205	20.193	$15.61^{+0.32}_{-0.20}$	20.205	11.1	10.8	12.8
VII Zw 118	151.36	25.99	0.0330 ± 0.0008	20.558	20.558	$18.84^{+0.10}_{-0.12}$	20.574	11.4	11.4	8.58
ESO350-IG38	328.06	-82.85	0.0096 ± 0.0001	20.201	20.157	NA	20.201	16.6	15.0	17.0
ESO572-G34	286.12	42.12	0.0340 ± 0.0004	20.410	20.410	NA	20.410	7.56	7.56	6.54
HE 0238-1904	200.48	-63.63	0.0272 ± 0.0011	20.417	20.368	NA	20.417	9.61	8.58	8.97
Mrk 487	87.84	49.03	0.0120 ± 0.0003	20.142	20.094	NA	20.142	11.6	10.3	8.66
NGC 4649	295.88	74.34	0.0226 ± 0.0006	20.297	20.297	NA	20.297	8.77	8.77	12.2
HE 1228+0131	291.26	63.66	0.0162 ± 0.0014	20.230	20.181	NA	20.230	10.5	9.37	10.1
HE 1326-0516	320.07	56.07	0.0256 ± 0.0006	20.331	20.308	NA	20.331	8.37	7.94	7.88
HS 1102+3441	188.56	66.22	0.0197 ± 0.0012	20.189	19.814	NA	20.189	7.85	7.85*	9.33
Mrk 36	201.36	66.49	0.0250 ± 0.0012	20.302	20.123	NA	20.302	8.01	5.31	8.79
Mrk 54	110.64	84.55	0.0129 ± 0.0004	20.110	20.110	NA	20.110	10.0	10.0	8.96
Mrk 59	111.54	82.12	0.0093 ± 0.0004	20.016	19.920	NA	20.016	11.2	11.2*	8.16
Mrk 487	82.84	49.03	0.0120 ± 0.0003	20.142	20.094	NA	20.094	11.6	10.3	9.33
Mrk 734	244.75	63.94	0.0267 ± 0.0011	20.385	20.251	NA	20.385	9.09	9.09*	9.79
Mrk 771	269.44	81.74	0.0233 ± 0.0003	20.377	20.159	NA	20.377	10.2	6.19	6.12
Mrk 829	58.76	63.25	0.0108 ± 0.0003	19.977	19.977	NA	19.977	8.79	8.79	7.99
Mrk 926	64.09	-58.76	0.0354 ± 0.0007	20.436	20.366	NA	20.436	7.70	6.56	10.9
Mrk 1502	123.75	-50.18	0.0559 ± 0.0018	20.669	20.669	NA	20.669	8.35	8.35	6.76
NGC 3504	204.60	-66.04	0.0228 ± 0.0002	20.294	19.628	NA	20.294	8.63	8.63*	10.2
NGC 3991	185.68	77.20	0.0189 ± 0.0002	20.217	19.966	NA	20.217	8.72	8.72*	9.73
NGC 5548	31.96	70.50	0.0168 ± 0.0009	20.203	20.203	NA	20.203	9.49	9.49	9.16
NGC 7496	347.84	-63.80	0.0084 ± 0.0001	20.133	20.114	NA	20.133	16.2	15.5	13.6
PG 0947+396	182.85	50.75	0.0162 ± 0.0006	20.224	20.079	NA	20.224	10.3	7.40	9.01
PG 1001+291	200.09	53.20	0.0190 ± 0.0005	20.249	19.801	NA	20.249	9.33	9.33*	8.83
PG 1004+130	225.12	49.12	0.0331 ± 0.0005	20.569	20.569	NA	20.569	11.2	11.2	9.21
PG 1048+342	190.60	63.44	0.0199 ± 0.0012	20.202	19.958	NA	20.202	8.00	8.00*	7.86
PG 1216+069	281.07	68.14	0.0186 ± 0.0007	20.209	20.209	NA	20.209	8.69	8.69	8.01
PG 1307+085	316.79	70.71	0.0292 ± 0.0008	20.341	20.324	NA	20.341	7.51	7.23	7.87
PG 1352+183	4.37	72.87	0.0159 ± 0.0006	20.223	20.223	NA	20.223	10.5	10.5	10.7
PG 1402+261	32.96	73.46	0.0132 ± 0.0004	20.158	20.158	NA	20.158	10.9	10.9	9.89
PG 1404+226	21.48	72.37	0.0190 ± 0.0003	20.309	20.271	NA	20.309	10.7	9.82	9.96
PG 1411+442	83.83	66.35	0.0084 ± 0.0012	19.880	19.857	NA	19.880	9.04	8.57	6.54
PG 1415+451	84.72	65.32	0.0071 ± 0.0003	19.816	19.739	NA	19.816	9.23	7.72	6.14

Table 1—Continued

AGN Name	ℓ (deg)	b (deg)	$E(B - V)$ (SF11)	$\log N_{\text{HI}}^{\text{b}}$ (all-v)	$\log N_{\text{HI}}^{\text{b}}$ (low-v)	$\log N_{\text{H}_2}^{\text{b}}$ (FUSE)	$\log N_{\text{H}}^{\text{b}}$ (total)	Ratio ^c (all-v)	Ratio ^c (low-v)	GN-Ratio ^c (all-v)
(1)	(2)	(3)	(4)	(5)	(6)	(7)	(8)	(9)	(10)	(11)
PG 1444+407	69.90	62.72	0.0114 ± 0.0004	20.031	19.866	NA	20.031	9.43	6.45	6.69
PG 2349-014	91.66	-60.36	0.0234 ± 0.0004	20.483	20.478	NA	20.483	13.0	12.9	9.37
SBS 0335-052	191.34	-44.69	0.0402 ± 0.0015	20.556	20.556	NA	20.556	8.94	8.94	7.40
SBS 1415+437	81.96	66.20	0.0077 ± 0.0003	20.021	19.920	NA	20.021	13.6	10.8	9.39
Tol 0440-381	241.07	-40.98	0.0130 ± 0.0005	20.331	20.331	NA	20.331	16.5	16.5	13.0
Ton 1187	188.33	55.38	0.0093 ± 0.0008	20.076	19.862	NA	20.076	12.8	7.83	12.0
vZ 1128	42.50	78.68	0.0117 ± 0.0005	20.037	20.037	NA	20.037	9.30	9.30	9.36

^aAGN sight lines surveyed in H I 21-cm emission (Wakker et al. 2003). Values of $\log N_{\text{HI}}$ for NGC 1068 are correct; they were incorrectly transcribed in Gillmon et al. (2006). The first 55 AGN also have H₂ column densities measured with FUSE ultraviolet spectra, with some survey duplications: 38 in Gillmon et al. (2006), 18 in Wakker (2006), 8 in Collins et al. (2003), one (Fairall 9) in Richter et al. (2001b) and one (HE 0226-4110) in both Fox et al. (2005) and Wakker et al. (2006). See Appendix B for more details. The next 39 AGN only have H I measurements. Columns 1–3 provide AGN name and Galactic coordinates. Column 4 gives the FIR-inferred $E(B - V)$ from SF11, as tabulated on the IRAC/IRSA website. Column 5 lists H I column densities ($\log N_{\text{HI}}$) for all velocities (Wakker et al. 2003), and column 6 gives H I excluding HVCs and most IVCs. Column 7 gives H₂ column densities, and column 8 gives values of $N_{\text{H}} = N_{\text{HI}} + 2N_{\text{H}_2}$ at all velocities. The last three columns present ratios $N_{\text{H}}/E(B - V)$ in units $10^{21} \text{ cm}^{-2} \text{ mag}^{-1}$. Column 9 presents ratios for gas at all velocities and SF11 reddening. Column 10 shows ratios for low-velocity gas (SF11 reddening) except when marked with an asterisk for inclusion of strong IVCs. Column 11 gives the all-velocities ratio, using $E(B - V)$ from Planck-GN. Ratios for 11 sight lines with $E(B - V)$ shown in boldface have uncertain $E(B - V) < 0.01$ (SF11).

^bColumn 5 lists low-velocity values after subtracting HVCs and most IVCs. Several sight lines pass through strong IVCs (IV Arch, IV18, IV19, IV26, S1) some of which are important contributors to the total H I (see notes in text). With H₂ detected in absorption they likely contain dust. The gas-to-dust ratios for these sight lines are computed with N_{HI} that includes the IVCs, marked with asterisks (Column 10). Most high-latitude sight lines exhibit ratios higher than the mean value, $\langle N_{\text{H}}/E(B - V) \rangle \approx 6 \times 10^{21} \text{ cm}^{-2} \text{ mag}^{-1}$, measured toward OB stars in the Galactic disk (Bohlin et al. 1978; Shull et al. 2021).

^cWe list three values of $N_{\text{H}}/E(B - V)$, two with $E(B - V)$ from SF11 (columns 9 and 10) and one using Planck GN (column 11). Columns 9 and 11 include gas at all velocities, while column 10 uses gas at low velocities only. In 17 cases, noted by asterisks, we included strong IVCs with the low velocity gas.

Table 2. Comparison of H I Column Densities^a

AGN Name	$\log N_{\text{HI}}$ (LAB)	$\log N_{\text{HI}}$ (GB)	$\log N_{\text{HI}}$ (GBT)	$\log N_{\text{HI}}$ (Wak03)	$\log N_{\text{HI}}$ (HI4PI)	$\Delta \log N_{\text{HI}}$ (3)–(4)	$\Delta \log N_{\text{HI}}$ (5)–(4)	$\Delta \log N_{\text{HI}}$ (6)–(4)
(1)	(2)	(3)	(4)	(5)	(6)	(7)	(8)	(9)
3C 249.1	20.400	20.431 ± 0.013	20.414 ± 0.013	20.446 (GB)	20.452	+0.017	+0.032	+0.038
3C 273	20.169	20.184 ± 0.021	20.108 ± 0.032	20.222 (GB)	20.231	+0.076	+0.114	+0.123
H1821+643	20.528	...	20.536 ± 0.011	20.584 (Eff)	20.549	...	+0.048	+0.013
HE 0226-4110	20.171	...	20.114 ± 0.010	20.272 (VE)	20.165	...	+0.158	+0.051
HS 0624+6907	20.791	...	20.781 ± 0.024	20.898 (Eff)	20.802	...	+0.117	+0.021
MRC 2251-178	20.374	20.415 ± 0.016	20.390 ± 0.014	20.415 (GB)	20.425	+0.025	+0.025	+0.035
Mrk 205	20.436	...	20.463 ± 0.012	20.508 (Eff)	20.468	...	+0.045	+0.005
Mrk 279	20.128	20.216 ± 0.019	20.193 ± 0.020	20.338 (Eff)	20.104	+0.023	+0.145	−0.089
Mrk 335	20.496	20.555 ± 0.015	20.477 ± 0.015	20.567 (GB)	20.517	+0.078	+0.090	+0.040
Mrk 478	19.916	19.913 ± 0.040	19.927 ± 0.035	20.010 (GB)	19.956	−0.014	+0.083	+0.029
Mrk 509	20.613	20.617 ± 0.013	20.583 ± 0.012	20.613 (GB)	20.594	+0.034	+0.030	+0.011
Mrk 771	20.415	20.357 ± 0.016	20.327 ± 0.016	20.377 (GB)	20.355	+0.030	+0.050	+0.028
Mrk 876	20.346	20.424 ± 0.013	20.395 ± 0.015	20.424 (Eff)	20.372	+0.029	+0.029	−0.023
Mrk 926	20.413	20.417 ± 0.015	...	20.436 (GB)	20.458
Mrk 1383	20.387	20.382 ± 0.017	20.370 ± 0.017	20.547 (GB)	20.412	+0.012	+0.177	+0.042
Mrk 1513	20.550	20.544 ± 0.013	20.534 ± 0.013	20.555 (GB)	20.569	+0.010	+0.021	+0.035
NGC 985	20.537	20.546 ± 0.014	20.534 ± 0.015	20.522 (GB)	20.546	+0.012	−0.012	+0.012
NGC 5548	20.131	20.172 ± 0.022	20.164 ± 0.021	20.203 (GB)	20.190	+0.008	+0.039	+0.026
NGC 7469	20.654	20.643 ± 0.021	20.637 ± 0.022	20.649 (Eff)	20.654	+0.006	+0.012	+0.017
PG 0804+761	20.497	20.525 ± 0.016	20.514 ± 0.017	20.588 (Eff)	20.524	+0.011	+0.074	+0.010
PG 0953+414	19.997	20.039 ± 0.028	19.995 ± 0.020	20.087 (Eff)	20.028	+0.044	+0.092	+0.033
PG 1001+291	20.203	20.210 ± 0.019	20.195 ± 0.019	20.249 (GB)	20.244	+0.015	+0.054	+0.049
PG 1116+215	20.065	20.084 ± 0.035	20.072 ± 0.020	20.075 (Eff)	20.086	+0.012	+0.003	+0.014
PG 1211+143	20.413	20.410 ± 0.015	20.413 ± 0.013	20.421 (GB)	20.425	−0.003	+0.008	+0.012
PG 1216+069	20.173	20.173 ± 0.026	20.163 ± 0.021	20.209 (GB)	20.182	+0.010	+0.046	+0.019
PG 1259+593	19.983	20.168 ± 0.037	20.247 ± 0.020	20.225 (Eff)	20.150	−0.079	−0.022	−0.097
PG 1302-102	20.497	20.485 ± 0.014	20.455 ± 0.015	20.502 (GB)	20.494	+0.030	+0.047	+0.039
PG 1351+640	20.301	20.401 ± 0.021	20.419 ± 0.022	20.441 (Eff)	20.341	−0.018	+0.022	−0.078
PG 1444+407	20.008	20.037 ± 0.028	20.022 ± 0.029	20.031 (GB)	20.036	+0.015	+0.009	+0.014
PHL 1811	20.606	...	20.599 ± 0.019	20.592 (LDS)	20.628	...	−0.007	+0.029
PKS 0405-12	20.508	20.531 ± 0.014	20.509 ± 0.013	20.537 (GB)	20.541	+0.022	+0.028	+0.032
PKS 2005-489	20.575	20.655 (VE)	20.561
PKS 2155-304	20.117	20.092 ± 0.026	20.053 ± 0.020	20.123 (Eff)	20.102	+0.039	+0.070	+0.049
Ton S180	20.104	20.035 ± 0.055	20.031 ± 0.028	20.097 (GB)	20.122	+0.004	+0.066	+0.091
Ton S210	20.129	...	20.137 ± 0.010	20.205 (Eff)	20.170	...	+0.068	+0.033
VII Zw 118	20.543	20.564 ± 0.015	20.539 ± 0.015	20.558 (GB)	20.576	+0.025	+0.019	+0.037

^aSample of 36 AGN sight lines surveyed in 21-cm emission at radio telescopes with different beam sizes. Columns 2–4 list H I column densities $\log N_{\text{HI}}$ (N_{HI} in cm^{-2}) from LAB, GB, GBT in Wakker et al. (2011). Additional GBT data in column 4 were provided by Jay Lockman (for Mrk 279, PG 1116+215, PG 1259+593, PKS 2155-304) and by Bart Wakker (for HE 0226-4110 and Ton S210). Columns 5 and 6 list values for gas at all velocities (Wakker et al. 2003) and HI4PI survey. Telescope labels are: Leiden-Argentina-Bonn (LAB), Green Bank 140-ft (GB), 100-m Green Bank Telescope (GBT), Leiden-Dwingeloo Survey (LDS), Effelsberg (Eff), Villa Elisa (VE) with beam sizes: LAB (36'), LDS (35'), VE (34'), GB (21'), HI4PI (16'), Eff (9.7'), GBT (9.1'). Columns 7, 8, and 9 show differences $\Delta \log N_{\text{HI}}$ relative to GBT in measurements from GB, Wakker et al. (2003), and HI4PI, respectively. Values differing by more than 0.050 (dex) are highlighted in boldface. The mean differences in $\log N_{\text{HI}}$ from GBT values are: +0.017 (GB-140 ft), +0.059 (Wakker et al. 2003), and +0.023 (HI4PI).

Table 3. Nine AGN with Significant Molecular Fractions^a

AGN Name	b	$E(B - V)$ (SF11 mag)	$\log N_{\text{H}}$ ($N_{\text{H}} \text{ cm}^{-2}$)	f_{H_2}
NGC 1068	-51.93	0.0289 ± 0.0004	20.440	0.0098
PG 1351+640	+52.02	0.0177 ± 0.0003	20.448	0.0156
PG 1211+143	+74.32	0.0286 ± 0.0011	20.429	0.0179
Mrk 335	-41.42	0.0305 ± 0.0031	20.583	0.0353
NGC 7714	-55.56	0.0451 ± 0.0002	20.690	0.0356
Mrk 116	+44.84	0.0292 ± 0.0028	20.537	0.0715
PHL 1811	-44.81	0.0415 ± 0.0031	20.640	0.105
NGC 3310	+54.06	0.0192 ± 0.0005	20.227	0.164
NGC 7469	-45.47	0.0599 ± 0.0015	20.732	0.173

^aNine high-latitude AGN ($|b| \geq 40^\circ$) from group 1 with molecular fractions greater than 1%. Galactic latitudes (b), $E(B - V)$, and total hydrogen column densities N_{H} are from Table 1. Molecular fractions $f_{\text{H}_2} \equiv 2N_{\text{H}_2}/N_{\text{H}}$ often exceed 1% when $\log N_{\text{H}} > 20.38 \pm 0.13$, the atomic-to-molecular transition seen toward high-latitude AGN (Gillmon et al. 2006).

Table 4. Dust Emission Model Parameters^a

Paper	Data Set	T_d (K)	Index β	Comments
SFD98	IRAS/DIRBE	18.2	2.0	Calibrated on elliptical galaxies
SF11	Recalibration	18.2	2.0	Calibrated on SDSS stars
Planck 2011	Planck-HIFI	17.9(0.9)	1.78(0.18)	Anticorrelation $\beta \propto T_d^{-2/3}$
Planck 2014	Planck-HIFI	20.3(1.3)	1.59(0.12)	Values at $ b > 15^\circ$
Planck 2016	Planck-HIFI	19.4(1.5)	1.63(0.17)	Values at $ b > 20^\circ$ (353 GHz)
Planck 2020	Planck HIFI	19.6	1.55(0.05)	Polarized dust emission
Casandjian 2022	IRAS/Planck	20.2	1.4	Excess dust at low N_{HI}

^aMean values of dust temperature T_d , with dispersion (1σ) in parentheses, and emissivity index (β) measured or assumed in a sample of FIR papers: Schlegel et al. (1998), Schlafly & Finkbeiner (2011), Casandjian et al. (2022), and four papers from the Planck Collaboration (listed in references). Meisner & Finkbeiner (2015) explored a two-temperature model with “hot dust” ($T_2 \approx 16.2$ K, $\beta_2 = 1.67$) and “cold dust” ($T_1 \approx 9.15$ K, $\beta_1 = 2.70$).

Table 5. Far-IR, E(B-V), and Dust Temperatures^a

AGN Name	$I(100\ \mu\text{m})$ (MJy/sr)	$E(B-V)$ (mag)	$I(100)/E(B-V)$ (MJy/sr/mag)	T_d (K)
3C 249.1	1.66 ± 0.11	0.0301 ± 0.0020	55.0 ± 5.2	17.861 ± 0.006
3C 273	1.04 ± 0.03	0.0179 ± 0.0004	58.1 ± 2.1	17.978 ± 0.013
ESO 141-G55	5.09 ± 0.30	0.0944 ± 0.0062	53.9 ± 4.8	17.861 ± 0.006
Fairall 9	1.13 ± 0.06	0.0217 ± 0.0011	52.1 ± 3.7	17.740 ± 0.011
H1821+643	2.14 ± 0.03	0.0370 ± 0.0007	57.8 ± 1.4	17.974 ± 0.019
HE 0226-4110	0.75 ± 0.03	0.0132 ± 0.0005	56.7 ± 3.1	17.939 ± 0.014
HE 1143-1810	1.82 ± 0.03	0.0331 ± 0.0005	55.0 ± 1.2	17.856 ± 0.010
HS 0624+6907	3.53 ± 0.08	0.0845 ± 0.0021	41.8 ± 1.4	17.278 ± 0.017
MRC 2251-178	1.87 ± 0.06	0.0335 ± 0.0011	55.8 ± 2.6	17.893 ± 0.004
Mrk 9	2.40 ± 0.08	0.0503 ± 0.0015	47.7 ± 2.1	17.550 ± 0.010
Mrk 106	1.25 ± 0.05	0.0235 ± 0.0010	53.2 ± 3.1	17.780 ± 0.009
Mrk 116	1.68 ± 0.16	0.0292 ± 0.0028	57.5 ± 7.8	17.966 ± 0.006
Mrk 205	1.82 ± 0.06	0.0344 ± 0.0011	52.9 ± 2.4	17.781 ± 0.009
Mrk 209	0.68 ± 0.03	0.0122 ± 0.0005	55.3 ± 3.3	17.876 ± 0.005
Mrk 279	0.80 ± 0.03	0.0138 ± 0.0005	57.9 ± 3.0	17.969 ± 0.005
Mrk 290	0.66 ± 0.05	0.0120 ± 0.0008	55.0 ± 5.6	17.871 ± 0.004
Mrk 335	1.58 ± 0.16	0.0305 ± 0.0031	51.8 ± 7.4	17.734 ± 0.013
Mrk 421	0.73 ± 0.06	0.0130 ± 0.0011	56.0 ± 6.6	17.893 ± 0.003
Mrk 478	0.64 ± 0.06	0.0111 ± 0.0009	57.3 ± 7.1	17.945 ± 0.005
Mrk 501	0.87 ± 0.02	0.0164 ± 0.0003	53.0 ± 1.6	17.782 ± 0.015
Mrk 509	2.76 ± 0.03	0.0492 ± 0.0005	56.0 ± 0.8	17.905 ± 0.005
Mrk 817	0.34 ± 0.01	0.0059 ± 0.0002	57.2 ± 2.6	17.948 ± 0.003
Mrk 876	1.38 ± 0.06	0.0230 ± 0.0009	59.8 ± 2.3	18.049 ± 0.006
Mrk 1095	5.61 ± 0.11	0.1099 ± 0.0017	51.1 ± 1.3	17.700 ± 0.005
Mrk 1383	1.78 ± 0.06	0.0276 ± 0.0009	64.5 ± 3.0	18.216 ± 0.009
Mrk 1513	2.07 ± 0.09	0.0370 ± 0.0017	55.9 ± 3.8	17.900 ± 0.013
MS 0700.7+6338	1.87 ± 0.04	0.0448 ± 0.0014	41.8 ± 1.6	17.273 ± 0.020
NGC 985	1.60 ± 0.02	0.0282 ± 0.0003	56.7 ± 0.9	17.931 ± 0.019
NGC 1068	2.28 ± 0.02	0.0289 ± 0.0004	78.7 ± 1.3	18.709 ± 0.017
NGC 1399	0.60 ± 0.02	0.0109 ± 0.0004	54.8 ± 2.7	17.541 ± 0.004
NGC 1705	0.40 ± 0.03	0.0070 ± 0.0005	57.8 ± 6.0	17.980 ± 0.002
NGC 3310	1.12 ± 0.03	0.0192 ± 0.0005	58.3 ± 2.2	17.992 ± 0.010
NGC 3690	0.83 ± 0.02	0.0144 ± 0.0002	57.7 ± 1.6	17.966 ± 0.010
NGC 4151	1.45 ± 0.07	0.0237 ± 0.0011	61.3 ± 4.1	18.103 ± 0.010
NGC 4214	1.17 ± 0.02	0.0187 ± 0.0003	62.8 ± 1.5	18.154 ± 0.014
NGC 4670	0.75 ± 0.02	0.0128 ± 0.0003	58.6 ± 2.1	18.013 ± 0.006
NGC 7469	2.92 ± 0.07	0.0599 ± 0.0015	48.7 ± 1.7	17.598 ± 0.024
NGC 7714	2.19 ± 0.01	0.0451 ± 0.0002	48.5 ± 0.3	17.588 ± 0.005
PG 0804+761	1.61 ± 0.03	0.0302 ± 0.0005	53.3 ± 1.3	17.793 ± 0.004
PG 0844+349	1.72 ± 0.05	0.0314 ± 0.0007	54.6 ± 2.0	17.848 ± 0.019
PG 0953+414	0.57 ± 0.03	0.0102 ± 0.0006	55.7 ± 4.4	17.898 ± 0.001
PG 1116+215	1.13 ± 0.01	0.0193 ± 0.0001	58.5 ± 0.6	18.001 ± 0.003
PG 1211+143	1.76 ± 0.06	0.0286 ± 0.0011	61.6 ± 3.2	18.118 ± 0.022
PG 1259+593	0.41 ± 0.02	0.0070 ± 0.0004	58.6 ± 4.4	17.995 ± 0.003

Table 5—Continued

AGN Name	$I(100 \mu\text{m})$ (MJy/sr)	$E(B - V)$ (mag)	$I(100)/E(B - V)$ (MJy/sr/mag)	T_d (K)
PG 1302-102	2.38 ± 0.06	0.0376 ± 0.0009	63.2 ± 2.2	18.172 ± 0.003
PG 1351+640	1.15 ± 0.03	0.0177 ± 0.0003	65.0 ± 2.0	18.237 ± 0.016
PG 1626+554	0.29 ± 0.03	0.0053 ± 0.0005	55.3 ± 7.7	17.877 ± 0.012
PHL 1811	2.15 ± 0.15	0.0415 ± 0.0031	51.8 ± 5.3	17.733 ± 0.012
PKS 0405-12	2.74 ± 0.20	0.0503 ± 0.0036	54.6 ± 5.6	17.845 ± 0.008
PKS 0558-504	2.37 ± 0.07	0.0388 ± 0.0012	61.2 ± 2.6	18.105 ± 0.007
PKS 2005-489	2.94 ± 0.03	0.0479 ± 0.0007	61.4 ± 1.1	18.108 ± 0.012
PKS 2155-304	1.10 ± 0.03	0.0185 ± 0.0005	59.3 ± 2.3	18.036 ± 0.010
Ton S180	0.72 ± 0.02	0.0123 ± 0.0002	58.1 ± 1.9	17.982 ± 0.002
Ton S210	0.84 ± 0.03	0.0144 ± 0.0004	58.2 ± 2.6	17.987 ± 0.003
VII Zw 118	1.62 ± 0.04	0.0330 ± 0.0008	49.2 ± 1.7	17.624 ± 0.008
ESO350-IG38	0.55 ± 0.01	0.0096 ± 0.0001	57.8 ± 1.0	17.969 ± 0.001
ESO572-G34	1.87 ± 0.03	0.0340 ± 0.0004	54.9 ± 1.0	17.862 ± 0.009
HE 0238-1904	1.54 ± 0.06	0.0272 ± 0.0011	56.5 ± 3.2	17.922 ± 0.063
Mrk 487	0.67 ± 0.02	0.0120 ± 0.0003	55.8 ± 2.1	17.894 ± 0.006
NGC 4649	1.38 ± 0.04	0.0226 ± 0.0006	61.0 ± 2.4	18.094 ± 0.012
HE 1228+0131	0.95 ± 0.08	0.0162 ± 0.0014	54.5 ± 6.6	18.017 ± 0.010
HE 1326-0516	1.64 ± 0.04	0.0256 ± 0.0006	64.1 ± 2.2	18.213 ± 0.006
HS 1102+3441	1.11 ± 0.07	0.0197 ± 0.0012	56.5 ± 4.8	17.925 ± 0.004
Mrk 36	1.48 ± 0.07	0.0250 ± 0.0012	59.1 ± 4.0	18.028 ± 0.002
Mrk 54	0.73 ± 0.02	0.0129 ± 0.0004	56.7 ± 2.3	17.928 ± 0.025
Mrk 59	0.53 ± 0.02	0.0093 ± 0.0004	57.3 ± 3.5	17.950 ± 0.005
Mrk 487	0.67 ± 0.02	0.0120 ± 0.0003	55.8 ± 2.1	17.894 ± 0.006
Mrk 734	1.49 ± 0.06	0.0267 ± 0.0011	55.8 ± 3.2	17.892 ± 0.004
Mrk 771	1.24 ± 0.02	0.0233 ± 0.0003	53.3 ± 1.0	17.794 ± 0.007
Mrk 829	0.61 ± 0.01	0.0108 ± 0.0003	56.2 ± 2.0	17.917 ± 0.004
Mrk 926	2.07 ± 0.04	0.0354 ± 0.0007	58.5 ± 1.6	17.997 ± 0.006
Mrk 1502	2.55 ± 0.08	0.0559 ± 0.0018	45.6 ± 2.0	17.455 ± 0.003
NGC 3504	1.32 ± 0.01	0.0228 ± 0.0002	58.1 ± 0.7	17.991 ± 0.008
NGC 3991	1.06 ± 0.01	0.0189 ± 0.0002	56.1 ± 0.9	17.901 ± 0.004
NGC 5548	0.92 ± 0.05	0.0168 ± 0.0009	54.5 ± 4.1	17.838 ± 0.005
NGC 7496	0.47 ± 0.01	0.0084 ± 0.0001	55.9 ± 1.0	17.887 ± 0.003
PG 0947+396	0.92 ± 0.04	0.0162 ± 0.0006	56.9 ± 3.1	17.943 ± 0.002
PG 1001+291	1.08 ± 0.03	0.0190 ± 0.0005	57.1 ± 2.0	17.924 ± 0.002
PG 1004+130	1.87 ± 0.02	0.0331 ± 0.0005	56.6 ± 1.1	17.928 ± 0.003
PG 1048+342	1.13 ± 0.07	0.0199 ± 0.0012	56.8 ± 5.0	17.933 ± 0.002
PG 1216+069	1.01 ± 0.04	0.0186 ± 0.0007	54.4 ± 2.9	17.845 ± 0.005
PG 1307+085	1.58 ± 0.05	0.0292 ± 0.0008	54.0 ± 2.2	17.823 ± 0.005
PG 1352+183	0.90 ± 0.04	0.0159 ± 0.0006	56.7 ± 3.1	17.931 ± 0.011
PG 1402+261	0.74 ± 0.02	0.0132 ± 0.0004	56.1 ± 2.4	17.907 ± 0.008
PG 1404+226	1.12 ± 0.02	0.0190 ± 0.0003	58.7 ± 1.3	18.007 ± 0.002
PG 1411+442	0.48 ± 0.07	0.0084 ± 0.0012	56.5 ± 11.7	17.927 ± 0.014
PG 1415+451	0.40 ± 0.02	0.0071 ± 0.0003	56.9 ± 3.4	17.928 ± 0.009
PG 1444+407	0.63 ± 0.02	0.0114 ± 0.0004	55.0 ± 2.8	17.855 ± 0.005

Table 5—Continued

AGN Name	$I(100 \mu\text{m})$ (MJy/sr)	$E(B - V)$ (mag)	$I(100)/E(B - V)$ (MJy/sr/mag)	T_d (K)
PG 2349-014	1.33 ± 0.02	0.0234 ± 0.0004	56.9 ± 1.3	17.921 ± 0.009
SBS 0335-052	2.05 ± 0.07	0.0402 ± 0.0015	51.0 ± 2.7	17.698 ± 0.012
SBS 1415+437	0.45 ± 0.02	0.0077 ± 0.0003	58.6 ± 3.4	18.007 ± 0.003
Tol 0440-381	0.67 ± 0.03	0.0130 ± 0.0005	51.2 ± 2.9	17.711 ± 0.012
Ton 1187	0.52 ± 0.04	0.0093 ± 0.0008	56.0 ± 6.7	17.894 ± 0.002
vZ 1128	0.66 ± 0.03	0.0117 ± 0.0005	56.1 ± 3.3	17.909 ± 0.002

^aFIR data (SF11) used to estimate the extinction toward 94 AGN in Table 1. The first 55 quasars have both H I and H₂ measurements; the next 39 have only H I. Columns 2 and 3 are the 100 μm surface brightness and FIR-inferred color excess, tabulated on the IPAC/IRSA website (<https://irsa.ipac.caltech.edu/applications/DUST>). Column 4 gives the ratio, $I(100 \mu\text{m})/E(B - V)$, with errors found from the relative errors on $I(100 \mu\text{m})$ and $E(B - V)$ added in quadrature. Column 5 gives the modeled dust temperature T_d . Several AGN sight lines have large errors on $I(100 \mu\text{m})$ and $E(B - V)$ with their ratios uncertain by 10-15%. For PG 1411+442, the uncertainty is 20%.

Table 6. Statistics of QSO Sub-samples^a

Sample	N_{QSO}	$\langle E(B - V) \rangle$ (SF11)	$\langle N_{\text{H}}/E(B - V) \rangle$ (all vel/SF11)	$\langle N_{\text{H}}/E(B - V) \rangle$ (low vel/SF11)	$\langle N_{\text{H}}/E(B - V) \rangle$ (all vel/Pl-GN)
(1)	(2)	(3)	(4)	(5)	(6)
Primary (H I, H ₂)	55	0.0295	11.53 ± 0.57	9.66 ± 0.34	10.59 ± 0.42
Modified	51	0.0313	10.64 ± 0.41	9.22 ± 0.27	10.30 ± 0.38
Complex C	9	0.0151	17.0 ± 5.2	10.7 ± 3.5	12.9 ± 4.3
Low-E(B-V)	4	0.0063	22.9	15.4	14.3
Secondary (H I)	39	0.0192	10.20 ± 0.38	9.37 ± 0.38	9.27 ± 0.35
Modified	32	0.0219	9.66 ± 0.34	9.03 ± 0.37	9.02 ± 0.27
Low-E(B-V)	7	0.0084	12.7	10.9	10.4

^aMean values of $E(B - V)$ and gas-to-dust ratios $\langle N_{\text{H}}/E(B - V) \rangle$ in units $10^{21} \text{ cm}^{-2} \text{ mag}^{-1}$ for various sub-samples of the 94 quasars. The mean ratios are shown for gas at all velocities (columns 4 and 6) and low velocity only ($|V_{\text{LSR}}| \leq 90 \text{ km s}^{-1}$) in column 5. Errors on the mean are evaluated as $\sigma/N^{1/2}$, where σ is the variance in sample of N targets. Ratios in columns 4 and 5 adopt $E(B - V)$ from SF11, while those in column 6 adopt Planck-GN. The primary group includes 55 QSOs with both H I and H₂ measurements. In the secondary group of 39 QSOs with only H I, the mean ratios are 12% lower, reflecting the missing contribution from H₂. In each group, the modified samples exclude sight lines with low (and uncertain) $E(B - V) < 0.01$ from SF11. Nine quasars behind HVC Complex C (Table 7) are among the 55 targets with both H I and H₂. Their elevated ratios exhibit large variations in FIR estimates of $E(B - V)$ from SF11 and Planck-GN.

Table 7. Ratios^a in High-Velocity Cloud Complex-C

QSO	$E(B - V)$ (SF11)	$E(B - V)$ (Pl-GN)	E -Ratio (GN/SF11)	Ratio-all (SF11)	Ratio-low (SF11)	Ratio-all (Pl-GN)	Ratio-low (Pl-GN)
(1)	(2)	(3)	(4)	(5)	(6)	(7)	(8)
Mrk 205	0.0344 ± 0.0011	0.0377 ± 0.0053	1.10	9.37	7.38	8.54	6.73
Mrk 279	0.0138 ± 0.0005	0.0154 ± 0.0002	1.12	15.8	6.11	14.2	5.49
Mrk 290	0.0120 ± 0.0008	0.0162 ± 0.0003	1.35	22.2	11.1	16.4	8.21
Mrk 501	0.0164 ± 0.0003	0.0183 ± 0.0004	1.11	12.6	10.6	11.3	9.54
Mrk 817	0.0059 ± 0.0002	0.0115 ± 0.0001	1.95	20.6	15.1	10.6	7.75
Mrk 876	0.0230 ± 0.0009	0.0291 ± 0.0006	1.26	11.5	7.05	9.14	5.57
PG 1259+593	0.0070 ± 0.0004	0.0086 ± 0.0001	1.23	24.0	11.2	19.5	5.43
PG 1351+640	0.0177 ± 0.0003	0.0156 ± 0.0001	0.88	15.9	11.2	18.0	12.7
PG 1626+554	0.0053 ± 0.0005	0.0137 ± 0.0002	2.59	21.3	16.3	8.24	6.28
Mean values	0.0151	0.0185		17.0	10.7	12.9	7.5

^aReddening values $E(B - V)$ and gas-to-dust ratios $N_{\text{H}}/E(B - V)$ (in $10^{21} \text{ cm}^{-2} \text{ mag}^{-1}$) for gas at all velocities and low velocity only toward nine sight lines to quasars behind HVC Complex C (Figure 2). Columns 2 and 3 list $E(B - V)$ from SF11 and Planck-GN (Planck Collaboration XLVIII 2016), with their ratio in column (4). Columns 5 and 6 list gas-to-dust ratios $N_{\text{H}}/E(B - V)$ based on SF11 reddening and gas at different velocities. Columns 7 and 8 list the ratios based on Planck-GN reddening. Mean values are listed at the bottom, spanning a range outside the errors. Mean values of $E(B - V)$ from Planck-GN are 22% higher than SF11, with most $E(B - V)$ ratios higher than SF11 values. Two sight lines have GN reddening 1.9–2.6 times larger than SF11, and only one of nine has a ratio less than 1.0. The mean low-velocity ($|V_{\text{LSR}}| < 90 \text{ km s}^{-1}$) gas-to-dust ratio is $\sim 60\%$ of that for gas at all velocities.

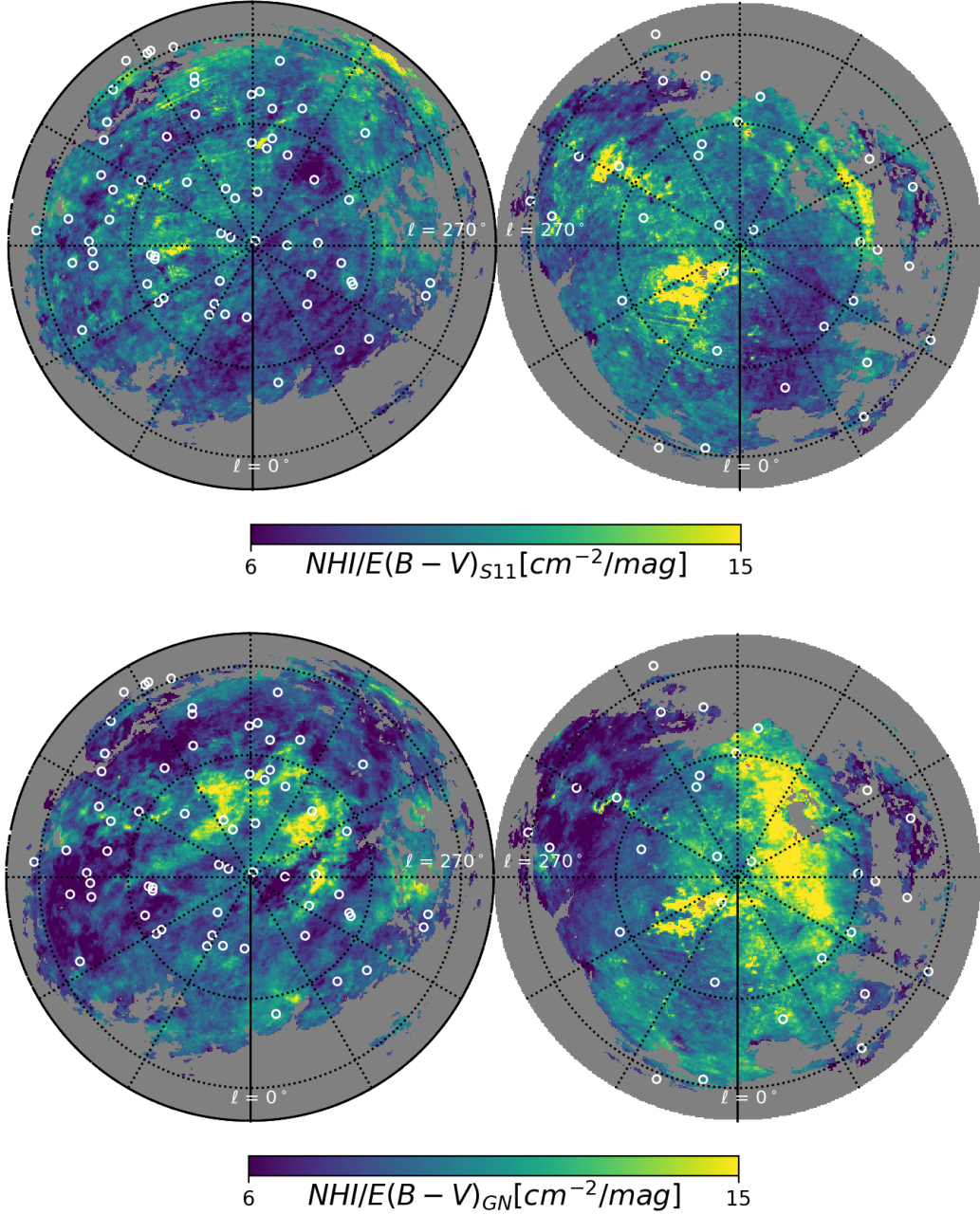


Fig. 1.— Polar projection maps of the ratio $N_{\text{HI}}/E(B - V)$ between N_{HI} from HI4PI for low-velocity gas with $|V_{\text{LSR}}| \leq 90 \text{ km s}^{-1}$ and $E(B - V)$ from SF11 (top) and Planck-GN (bottom). Locations of the 94 quasars are shown as white circles. Both reddening maps are smoothed to the HI4PI resolution of $16'$. Northern Galactic hemisphere is on the left, southern hemisphere on the right. Galactic longitude $\ell = 0^\circ$ is at the bottom and $\ell = 180^\circ$ at the top of each map. Longitude increases clockwise for northern hemisphere and counterclockwise for southern hemisphere, meeting at $\ell = 270^\circ$. Color scale at bottom shows gas-to-dust ratio in units $10^{21} \text{ cm}^{-2} \text{ mag}^{-1}$. The linear scale covers the 1st and 99th percentiles of the distribution of ratios of the top panel. White circles mark locations of 94 AGN.

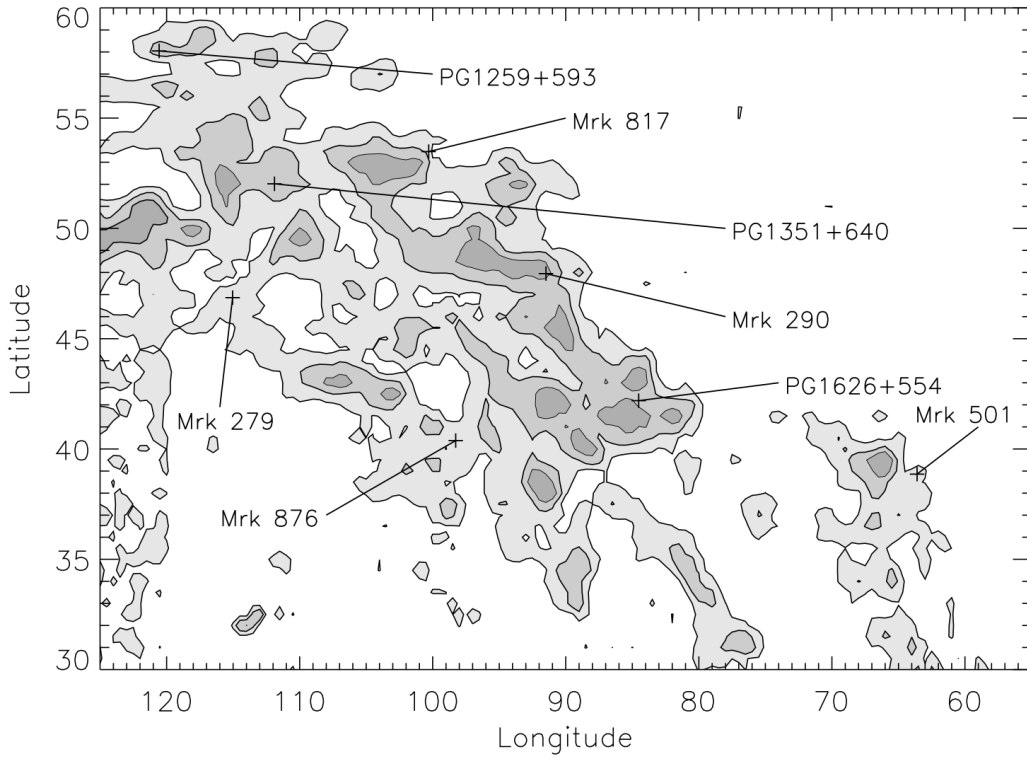


Fig. 2.— Contours of H I column density in Complex C from the Leiden-Dwingeloo Survey (Hartmann & Burton 1997) plotted on a 0.5 deg grid (35' beam) with H I contours at 1 , 3 , and $6 \times 10^{19} \text{ cm}^{-2}$. Locations of 8 of the 9 quasars in our study (Table 5) are labeled; Mrk 205 ($\ell = 125.45^\circ$, $b = 41.67^\circ$) lies just off the left side of the plot. Complex C extends over $\sim 2000 \text{ deg}^2$ in the Northern Galactic sky, with metallicity along these sight lines ranging from 0.1–0.3 solar (Collins et al. 2003, 2007).

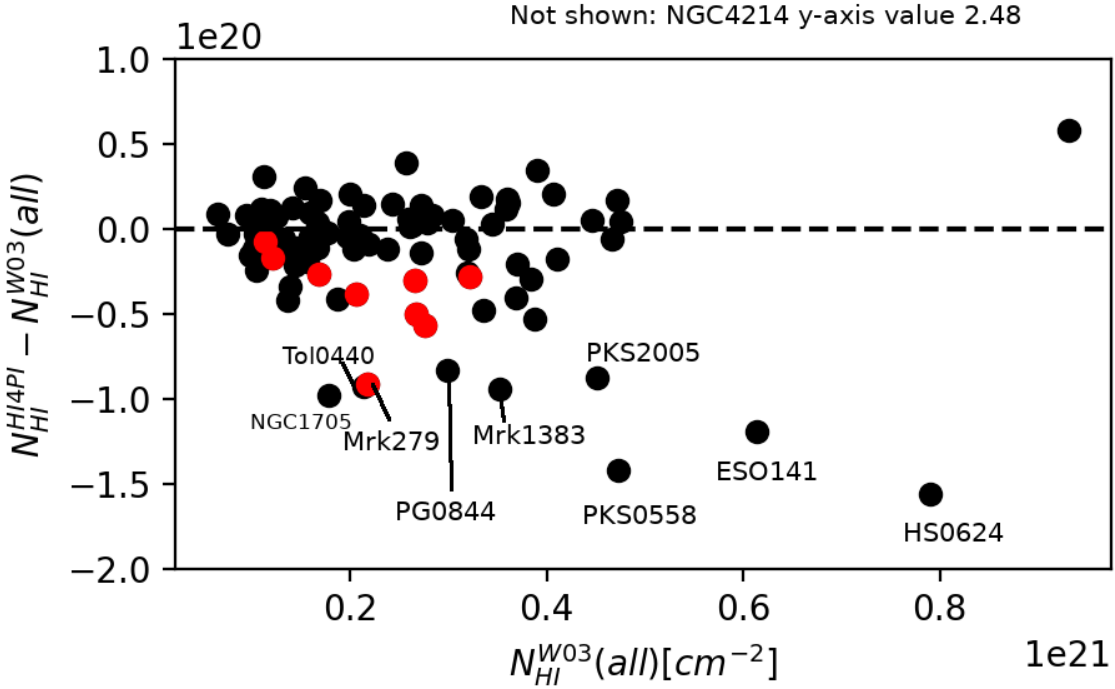


Fig. 3.— Differences in N_{HI} (at all velocities, in units of 10^{20} cm^{-2}) between HI4PI values (HI4PI Collaboration et al. 2016) and those from Wakker et al. (2003) from our Table 1. These are plotted versus N_{HI} (in units of 10^{21} cm^{-2}) from Table 1. Red points indicate nine sight lines passing through Complex C, an HVC with low dust content where H I makes a significant contribution to total N_{HI} . We have annotated several sight lines in which N_{HI} from HI4PI is considerably lower than that in Wakker et al. (2003). NGC 4214 is not shown, because its internal H I (at $+295 \text{ km s}^{-1}$) is included in the HI4PI velocity range.

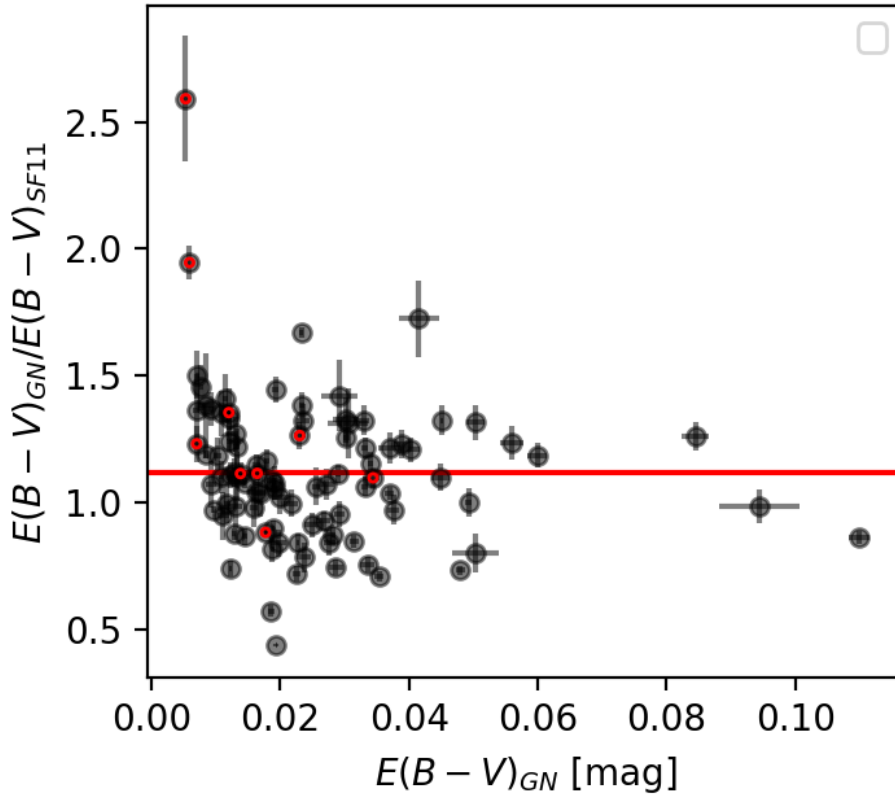


Fig. 4.— Distribution of ratios of $E(B - V)$ from Planck-GN and SF11. Values are from full sample (94 AGN), with nine QSOs behind HVC Complex C plotted in red. These include outliers (PG 1626+554 and Mrk 817) with anomalously high GN/SF11 ratios and very low $E(B - V)$. On average, the Planck-GN values are 12% higher than SF11, with considerable dispersion about the unweighted mean (red line), particularly in sight lines with $E(B - V) \lesssim 0.04$. The plotted errors are likely under-estimated owing to systematic effects in FIR modeling.

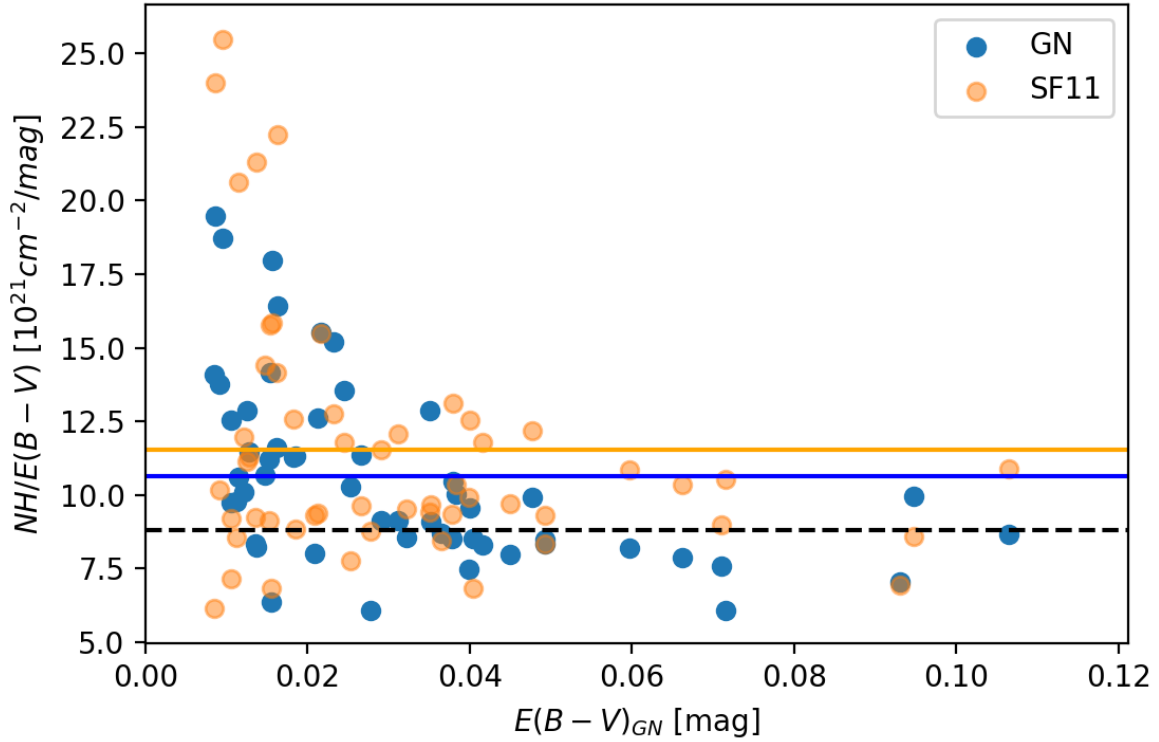


Fig. 5.— Gas-to-dust ratios (in $10^{21} \text{ cm}^{-2} \text{ mag}^{-1}$) using total hydrogen column density (N_{H}) for 55 AGN in our primary sample with both H I and H₂ (Table 1). The FIR-inferred $E(B - V)$ are plotted for both Planck-GN (blue circles) and SF11 (orange circles). Horizontal lines show the mean ratios of two distributions: 10.6 (blue solid line, Planck-GN), 11.5 (orange solid line, SF11). Black dotted line shows the mean ratio $N_{\text{HI}}/E(B - V) = 8.8$ from Lenz et al. (2017), which was based on just H I column densities.

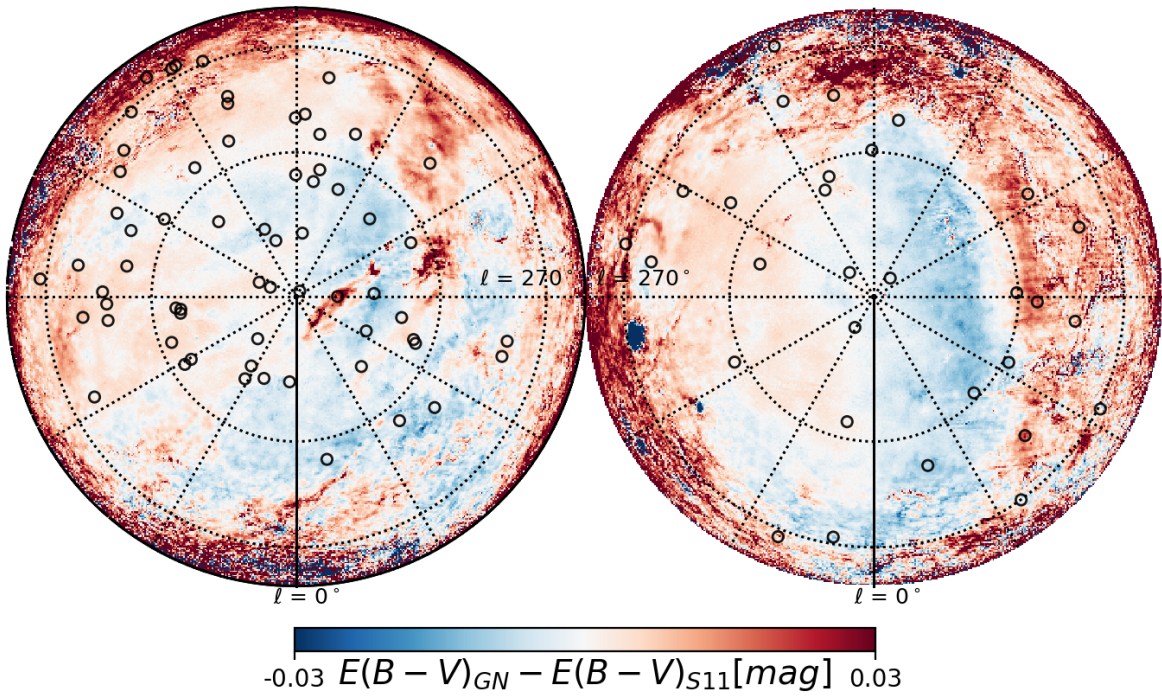


Fig. 6.— Polar projection maps showing the difference between $E(B - V)$ from Planck-GN and values from SF11. These variations track changes in the gas-to-dust ratio seen in the two ratio maps of Figure 1. For example, the red feature towards $(\ell, b) = (260 - 330^\circ, 80 - 84^\circ)$ is Markkanen’s Cloud (Markkanen 1979) with a discrepant dust emissivity spectral index β , as noted in Planck Collaboration XI (2014). Many IVCs also appear in these difference plots (see Section 3.3).

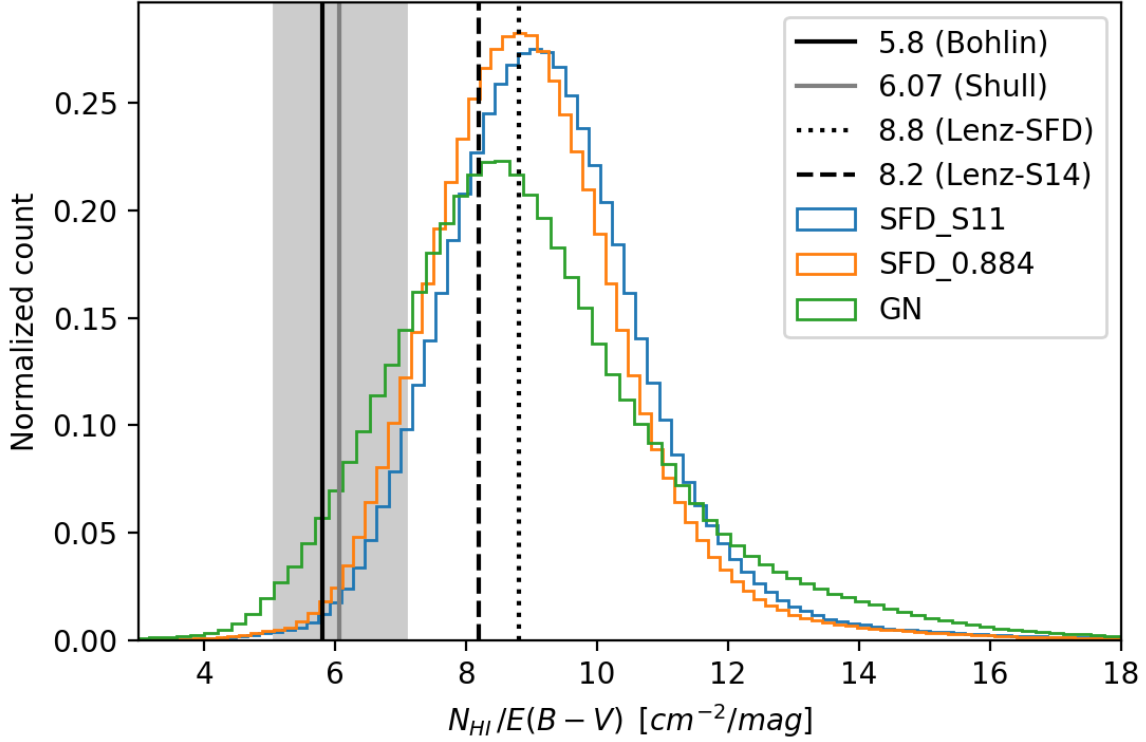


Fig. 7.— Comparison of distributions of gas-to-dust ratios over the high-latitude sky for three choices of reddening map (SFD98, SF11, Planck-GN). Here N_{HI} comes from HI4PI survey for gas at $|V_{\text{LSR}}| \leq 90 \text{ km s}^{-1}$. Reddening maps are smoothed to the HI4PI resolution ($16'$). In the label box, SFD-S11 refers to the standard 0.86 recalibration, and SFD-0.884 refers to recalibration with the Johnson bandpasses, consistent with Planck-GN analysis. Each histogram is normalized to unit area. Vertical lines show mean ratios determined in previous papers: 5.8 (Bohlin et al. 1978) and 6.07 (Shull et al. 2021) toward stars in the Galactic disk, and 8.8 and 8.2 quoted in Lenz et al. (2017) at high-latitude. Grey wash shows the (1σ) variance in the Shull et al. (2021) survey of 129 stars within 5 kpc.

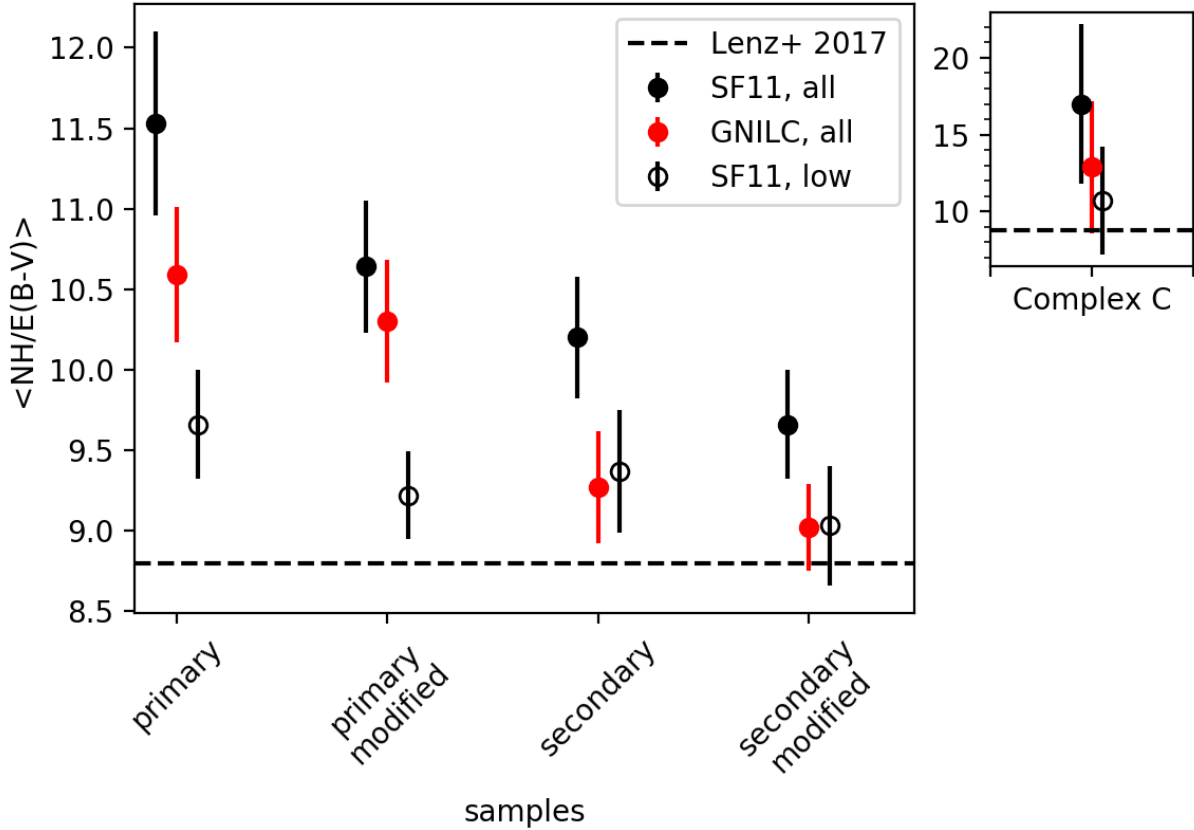


Fig. 8.— Summary of mean ratios $N_{\text{H}}/E(B - V)$ from our primary sample (group 1, 55 AGN) with both H I and H₂ measurements, and secondary sample (group 2, 39 AGN) with only H I. Modified samples exclude sight lines with uncertain reddening $E(B - V) < 0.01$ (see Table 6). Ratios are shown for two reddening maps (SF11 and Planck-GNILC) and for gas at low velocity and all velocities (including HVCs and IVCs). Nine sight lines through HVC Complex C with elevated ratios (low dust content) are a subset of the primary sample. The horizontal dotted line shows the mean ratio of $N_{\text{H}}/E(B - V) = 8.8$ at high latitude found by Lenz et al. (2017).